The Astronomical Journal, 168:290 (21pp), 2024 December https://doi.org/10.3847/1538-3881/ad84e0

Spectroscopic and Photometric Confirmation of 3 Globular and 14 Intermediate-age Clusters in the Irr II Galaxy NGC 3077

P. A. Ovando[1], Y. D. Mayya[1], L. H. Rodríguez-Merino[1], L. Lomelí-Nuñez[2], B. Cuevas-Otahola[3], D. Rosa-González[1], and L. Carrasco[1]
[1] Instituto Nacional de Astrofísica, Óptica y Electrónica, Luis Enrique Erro 1, Tonantzintla 72840, Puebla, Mexico; ydm@inaoep.mx
[2] Valongo Observatory, Federal University of Rio de Janeiro, Ladeira Pedro Antonio 43, Saude Rio de Janeiro, RJ, 20080-090, Brazil
[3] Departamento de Matemáticas-FCE, Benemérita Universidad Autónoma de Puebla, Puebla, 72570, Mexico
Received 2024 May 13; revised 2024 September 29; accepted 2024 October 1; published 2024 November 29

Abstract

We present the results from spectroscopic and photometric analysis of 17 globular cluster (GC) candidates in the Irr II galaxy NGC 3077. The GC candidates were selected on the Hubble Space Telescope images and were cleaned of foreground Galatic stars using the GAIA parameters. We carried out aperture photometry using the multiband archival images from the Sloan Digital Sky Survey, Two Micron All Sky Survey of all candidates, and low resolution ($R = 1000$) spectroscopic observations of 12 GC candidates and three suspected foreground stars using the Optical System for Imaging and Low-Intermediate-Resolution Integrated Spectroscopy/Multi-Object Spectra mode at the Gran Telescopio Canarias. Age, metallicity, and extinction values were determined using both spectroscopic and photometric data, independently. We find three of the 17 candidates are old (age > 10 Gyr), metal-poor ([Fe/H] < -1.0 dex), and massive (mass $> 10^5 M_\odot$) GCs with characteristics similar to the classical GCs in the Milky Way. The rest are intermediate-age clusters (IACs) with typical ages of 3–4 Gyr and in general metal-rich clusters. The radial velocities of both populations are within 100 km s^{-1} of the recessional velocity of the host galaxy. A relatively large population of IACs and low value of GC specific frequency ($S_N = 0.7$) suggest that the preinteraction galaxy was actively forming stars and star clusters, and is unlikely to be a dwarf elliptical as suggested in some previous works.

Unified Astronomy Thesaurus concepts: Globular star clusters (656); Amorphous irregular galaxies (37); Star clusters (1567)

1. Introduction

Globular clusters (GCs) are relics of early star formation in the Universe, hence their ages and metallicities, two parameters heavily dependent on the epoch and physical properties of their formation, put strong constraints on the formation history of galaxies (e.g., L. Searle & R. Zinn 1978; G. Kauffmann & S. D. M. White 1993; K. M. Ashman & S. E. Zepf 1998; J. P. Brodie & J. Strader 2006). Based on cosmological *N*-body simulations, K. Bekki et al. (2008) found that around ∼90% of GCs currently in haloes of galaxies are formed in low-mass galaxies at redshifts greater than 3. In recent years, simulations that incorporate formation and evolution of star clusters in cosmological galaxy formation models have reproduced observational properties of GC populations in spiral galaxies, such as the Milky Way and M31 (e.g., E-MOSAICS; J. Pfeffer et al. 2018). The majority of GCs are older than 10 Gyr, especially those formed in massive galaxies (D. A. VandenBerg et al. 2013). With the advent of the James Webb Space Telescope, it has been possible to directly detect GC-like objects forming at times as early as 460 Myr of the Big Bang (A. Adamo et al. 2024). Meanwhile, the metallicity distribution function in several massive early-type galaxies displays bimodality, and some even trimodality (e.g., M31; N. Caldwell & A. J. Romanowsky 2016; S. Wang et al. 2019). However, there exist cases where the metallicity distribution is consistent with a single peak, such as in NGC 5128 (S. E. Zepf & K. M. Ashman 1993) and NGC 1399 (J. P. Blakeslee et al. 2012).

The bimodal metallicity distribution can be understood by the two-phase galaxy formation scenario (L. Oser et al. 2010; D. A. Forbes et al. 2011; C. Usher et al. 2012; M. A. Beasley et al. 2018; K. A. Alamo-Martínez et al. 2021). In this model, the first phase consists of rapid in situ star formation in which most of the metal-rich population is formed in the central ∼10% of the present-day radius of galaxies. Galaxies grow in mass and radius in the second phase by the accretion of metal-poor dwarf galaxies. Metal-rich population can be formed in the host galaxy during this second phase, if the accreting galaxy is gas-rich. GCs are expected to form in each of these two phases of galaxy formation, with metal-rich and metal-poor GCs located in the inner and outer parts of the galaxies, respectively (J. Pfeffer et al. 2018; J. M. D. Kruijssen et al. 2019). The relative number of in situ and accreted GCs in the two phases depends on the present-day galaxy mass, with massive galaxies having a higher fraction of accreted material. In this scenario, low-mass galaxies (mass $\leqslant 10^{10} M_\odot$) are expected to have a higher fraction of old metal-rich GCs as compared to the massive galaxies. On the other hand, GCs in genuine dwarf galaxies are expected to be metal poor (G. Kauffmann & S. D. M. White 1993). Studies of age and metallicities of GC systems in low-mass galaxies are required to test these predictions of the cosmological simulations. We summarize below some of the existing attempts in this direction.

I. Y. Georgiev et al. (2008) carried out a photometric study of GCs in 19 Magellanic type dwarf irregular galaxies, the majority of which have colors similar to the old metal-poor GCs found in the

haloes of giant local galaxies. On the other hand, M. C. Parisi et al. (2014) found a higher fraction of younger GCs ($3 <$ Age/Gyr < 10) in the Small Magellanic Cloud (SMC). J. Strader et al. (2012) found an unusual abundance of luminous red star clusters in the dwarf Magallanic irregular galaxy NGC 4449. Some of the clusters have properties of the old GCs. They also found two clusters with unexpected abundance properties; the clusters were neither metal-poor ([Fe/H] $= -1.0$ dex) nor α-elements enhanced ([Mg/Fe] ~ -0.1 to -0.2). These unusual properties are confirmed by F. Annibali et al. (2018) who found the old GCs in the NGC 4449 to be of intermediate metallicities ($-1.2 \lesssim$ [Fe/H] $\lesssim -0.7$ dex), with subsolar [α/Fe] ratios ($-0.8 \lesssim$ [α/Fe] $\lesssim 0.1$; peak at ~ -0.4). These studies illustrate the diversity in the age and metallicity properties of GC systems in dwarf galaxies, highlighting the importance of detailed studies of star cluster systems in more low-mass galaxies.

The color-magnitude diagram (CMD) of the constituent stars with the best fitting of an isochrone is the most widely recognized and direct technique to estimate the age of a star cluster (e.g., P. W. Hodge et al. 1999; N. Bastian et al. 2016). However, star clusters located in galaxies beyond the Local Group cannot be resolved even when using images obtained with the Hubble Space Telescope (HST). Therefore, most extagalatic star cluster analysis depends on integrated-light measurements to determine ages and/or metallicities (e.g., J. B. Nantais & J. P. Huchra 2010; Y. D. Mayya et al. 2013; R. S. Asa'd 2014; F. Annibali et al. 2018; L. Lomelí-Núñez et al. 2024).

The well-known M81 group consists of more than 30 galaxies and is located 3.63 Mpc away (W. L. Freedman et al. 1994). The three brightest members of the group, namely M81, M82, and NGC 3077 (M81 triplet), were involved in a tidal interaction (J. M. van der Hulst 1979; M. S. Yun et al. 1994). This interaction occurred around 300 Myr ago (M. S. Yun 1999) and has triggered a large-scale star formation in the disk of M82 (Y. D. Mayya et al. 2006; L. H. Rodríguez-Merino et al. 2011), and is also likely responsible for the nuclear starburst activities in NGC 3077. It is a dusty late-type galaxy, currently witnessing intense star formation in the central 500 pc (Table 1 displays the basic properties of NGC 3077). Morphologically, it has been classified as an Irregular II (Irr II) galaxy (see E. Holmberg 1950; G. de Vaucouleurs 1959; O. K. Krienke & P. W. Hodge 1974). A total mass of $2 \times 10^{10} M_{\odot}$ (M. S. Yun 1999) puts this galaxy in the upper fringe of what can be considered as a low-mass galaxy.

The central starburst region of NGC 3077 is host to a rich population of young Super Star Clusters (SSCs; J. Harris et al. 2004; P. Notni et al. 2004). T. J. Davidge (2004, hereafter D04) used ground-based wide-field near-IR (NIR) images to identify 12 GC candidates located in the periphery of NGC 3077. It is still unclear if all these candidates belong to this galaxy or if they are part of other members of the M81 group. More recently, A. L. Chies-Santos et al. (2022) have elaborated a new catalog of 642 GC candidates located in the M81 triplet. However, they did not recover a significant population of GC candidates in NGC 3077. Similarly, J. Pan et al. (2022) used multiwavelength data to select GC candidates in the outer halo of the M81 group, finding three candidates associated to NGC 3077. Despite these studies, there is no consensus on the total number of GCs in this galaxy.

According to W. E. Harris & S. van den Bergh (1981) the number of GCs (N_{GC}) in a galaxy normalized by its luminosity is given by the specific frequency equation, $S_N = N_{GC} 10^{0.4(M_V+15)}$. The specific frequency associated to irregular galaxies (e.g., SMC and LMC) is $<S_N> = 0.5$ (W. E. Harris 1991). In the case of NGC 3077, based on the observed absolute visual magnitude of $M_V \sim -16$ mag (see Table 1), and on the estimated specific frequency for irregular galaxies, the expected number of GCs is $N_{GC} \sim 2$.

Table 1
Basic Properties of NGC 3077

Parameter	Value	References
Morphology Type	Irr II (I0)	(a, b)
Distance	3.63 Mpc	(c)
Angular size	$5'.4 \times 4'.5$	(d)
Linear size	5.6 kpc	
R_{25}	$2'.68$	(d)
Radial velocity (V_{hel})	14.09 km s^{-1}	(d)
Total mass	$2 \times 10^{10} M_{\odot}$	(e)
$(B - I)$	1.692 mag	(f)
M_V	-16.202 mag	(f)
H_I mass	$6.9 \times 10^8 M_{\odot}$	(e)
H_2 mass	$1.6 \times 10^6 M_{\odot}$	(g)
$E(B - V)_{MW}$	0.07 mag	(h)
E(F475W − F814W)	0.12 mag	(h, i)
Metallicity (Z)	0.02	(j)

References: (a) E. Holmberg (1950), (b) G. de Vaucouleurs (1959), (c) W. L. Freedman et al. (1994), (d) G. de Vaucouleurs et al. (1991), (e) M. S. Yun (1999), (f) W. Z. Wisniewski & D. E. Kleinmann (1968), (g) F. Walter et al. (2002), (h) D. J. Schlegel et al. (1998), (i) using J. A. Cardelli et al. (1989) extinction curve, (j) D. Calzetti et al. (2004).

In this paper, we present the results of a spectroscopic study of 15 GC candidates in NGC 3077, which is the first of its kind for this galaxy. The GC candidates were selected from a list of 21 objects obtained in a search of the Advanced Camera for Surveys (ACS) images of the HST observations. We further carried out multiband photometric analysis of all the candidates, with the goal of obtaining a complete census of the GCs in this low-mass galaxy. The work is organized as follows. In Section 2, we discuss in detail the criteria used to select a sample of GC candidates and describe new and existing observational data used in this work. In Section 3, we implement tests to reject foreground stars and non-GC-like objects from our catalog. The results from photometric/spectroscopic analysis are presented in Section 4. The results are discussed in Section 5. Finally, in Section 6, we give a summary and the conclusions.

2. Sample of GC Candidates, Photometric Data, and Spectroscopic Observations

2.1. The Sample of GC Candidates and Photometric Data

The sample of GC candidates was defined on the F435W, F606W, and F814W images taken using the ACS/WFC camera onboard the HST (proposal ID 10915, PI: Julianne Dalcaton) on 2006 September 21. The first three rows of Table 2 give the details of these observations. The central $\sim 100'' \times 100''$ of the galaxy has been earlier observed on 2001 May 22 with the Wide Field Planetary Camera 2 (WFPC2) in F300W (proposal ID 9144, PI: Daniela Calzetti; J. Harris et al. 2004). F300W being the bluest of the HST bands available for this galaxy, we used this image to carry out photometry on the

Table 2
HST and Multiband Images Used in this Work

Instrum. (1)	Band (2)	Central λ (3)	Scale (4)	ZP (5)	Exp. Time (6)
HST/ACS	F814W	8037	0.05	25.512	1622
HST/ACS	F606W	5961	0.05	26.399	1596
HST/ACS	F475W	4818	0.05	26.144	1570
HST/WFPC2	F300W	3266	0.10	19.433	2400
SDSS	u	3551	0.4	21.589	53.9
SDSS	g	4686	0.4	22.596	53.9
SDSS	r	6165	0.4	22.350	53.9
SDSS	i	7481	0.4	22.138	53.9
SDSS	z	8931	0.4	21.978	53.9
2MASS	J	12350	1.0	20.952	7.8
2MASS	H	16620	1.0	20.728	7.8
2MASS	K_s	21590	1.0	20.085	7.8

Note. (1) Telescope/camera, (2) filter/band, (3) central wavelength in (Å), (4) scale of plate in (arcsec pix^{-1}), (5) zero-point in VEGAMAG system, (6) exposure time in (s).

selected GC candidates in the limited field of view of the WFPC2 observations.

We used the SEXTRACTOR program (E. Bertin & S. Arnouts 1996) to select sources on the HST/ACS images. During the SEXTRACTOR run we saved a number of geometric and photometric parameters that allowed us to distinguish genuine GC candidates from stars and fake sources. The most important of them are: full width at half maximum (FWHM), AREA, which is the number of contiguous pixels above the detection threshold, ELLIPTICITY, as it is measured at the isophote corresponding to the detection threshold on the background subtracted image enclosing the AREA, and magnitudes in aperture of 0.″2 radius in all the filters. A source is considered a GC candidate if it satisfies the following criteria: FWHM $\geqslant$ 2.1 pixels, AREA $>$ 50 pixels, ELLIPTICITY $<$ 0.66 (not elongated), F814W $\leqslant$ 22 mag, and F475W $-$ F814W $\geqslant$ 1.5 mag. The FWHM of 2.1 pixels corresponds to the point-spread function (PSF) of the ACS images, and hence the first criterion separates stars from extended objects. This criterion is similar to the concentration index (CI) used in some studies (e.g., B. C. Whitmore et al. 2014; see also L. Lomeli-Nunez et al. 2022 for a comparison between the FWHM and CI-based selections). The subsequent selection criteria involving AREA, ELLIPTICITY, and F814W magnitude allow us to eliminate a vast number of false clusters formed from faint superposed stars. These criteria have been successfully used earlier to select SSCs on the HST/ACS images by Y. D. Mayya et al. (2008), M. Santiago-Cortés et al. (2010), and more recently L. Lomeli-Nunez et al. (2022). The last criterion, namely the color cut, corresponds to the color of metal-poor ($Z \lesssim 0.008$) Simple Stellar Populations (SSPs) models (L. Girardi et al. 2002, hereafter G02[4]) older than 3 Gyr, and hence is expected to reject relatively blue, and hence young clusters from our sample.

Given the large number of reddened young clusters in the dusty central starburst region (D. Calzetti et al. 2000), we restricted our search of GC candidates to areas outside 25″ (450 pc) from the galactic center ($\alpha = 10^{\rm h}03^{\rm m}19\overset{\rm s}{.}07$, $\delta = +68°44'02\overset{''}{.}1$). This resulted in a sample of 21 GC candidates. In Figure 1, we illustrate the selection criteria. In the left-hand panel we show all the SEXTRACTOR sources (points) in AREA versus FWHM diagram with the 21 selected GC candidates identified by filled red circles. The open red circles are red clusters located in the central region of radius = 25″, whereas the blue circles are bluer clusters, which are candidates to SSCs, and are not part of the discussion in this study. In the right-hand panel, we show all the candidates that passed the first four criteria that define a star cluster in a CMD. The SSP evolutionary loci corresponding to ages $>$3 Gyr are shown for two metallicities ($Z = 0.004$ and 0.008) and two cluster masses ($10^5\,M_\odot$ and $10^6\,M_\odot$). The color cut (F475W $-$ F814W $\geqslant$ 1.5 mag) corresponding to 3 Gyr population at $Z = 0.008$ separates blue SSC candidates from red GC candidates. The reddening vector for $A_V = 1$ mag using the J. A. Cardelli et al. (1989, hereafter C89) extinction curve with $R_V = 3.1$ is shown by the arrow.

Figure 2 shows the locations of the GC candidates in the galaxy. The RGB (F814W, F606W, and F475W) stamps of the GC candidates are displayed in the bottom part of this figure. SEXTRACTOR has provided the coordinates of the GC candidates. With this information at hand, we have employed the *phot* task of IRAF (D. Tody 1986) to perform the circular aperture photometry using a radius of 0.″2. Local sky values are subtracted from each aperture magnitude using the median sky in an annular region of inner radius 0.″8 and width 0.″2 around each object.

GCs are marginally resolved objects on the HST/ACS images, which implies the flux lying outside a fixed aperture radius of 0.″2 used to measure the magnitude depends on the size of the cluster, or in our case its proxy, the FWHM. This correction can be calculated using the growth curves for isolated clusters in the same image or using simulated clusters as in L. Lomeli-Nunez et al. (2022). Using the isolated blue and red clusters in the image, we found that growth curves reach asymptotic values at radius = 15 pixel. Based on these measured magnitudes at 15 pixels, we defined a FWHM-dependent aperture correction $\Delta m = 0.096 \times \mathrm{FWHM} - 0.048$, which we applied to both the F475W and F814W aperture magnitudes.

We calculated errors on each measured magnitude assuming Poisson noise from the object and the sky. The errors on the magnitudes are added in quadrature to calculate the error on colors. GAIA Data Release 3 (DR3: Gaia Collaboration et al. 2016; C. Babusiaux et al. 2023) was used to bring all images to a single astrometric system using the coordinates of field stars in GAIA. Table 3 shows the parameters measured of the GC candidates: coordinates (Columns 2 and 3), photometric data (Columns 4, 5, and 6), FWHM measured by IRAF (Column 7), the galactocentric distance is measured in the plane of the sky (Column 8), object type and the method are used to determine it (based on results of the next sections; Columns 9 and 10), and cross identification with previous studies when available (Column 11).

2.2. Multiband Ancillary Images Data

In order to perform an analysis of the GC candidates using a large interval of the wavelength range, the HST's photometry of the GC candidates were complemented with ground-based archival images from the Sloan Digital Sky Survey (SDSS; K. Abazajian et al. 2003) and Two Micron All Sky Survey (2MASS; M. F. Skrutskie et al. 2006) missions (see Table 2). We performed aperture photometry using *phot* of IRAF on

[4] http://stev.oapd.inaf.it/cgi-bin/cmd_3.1

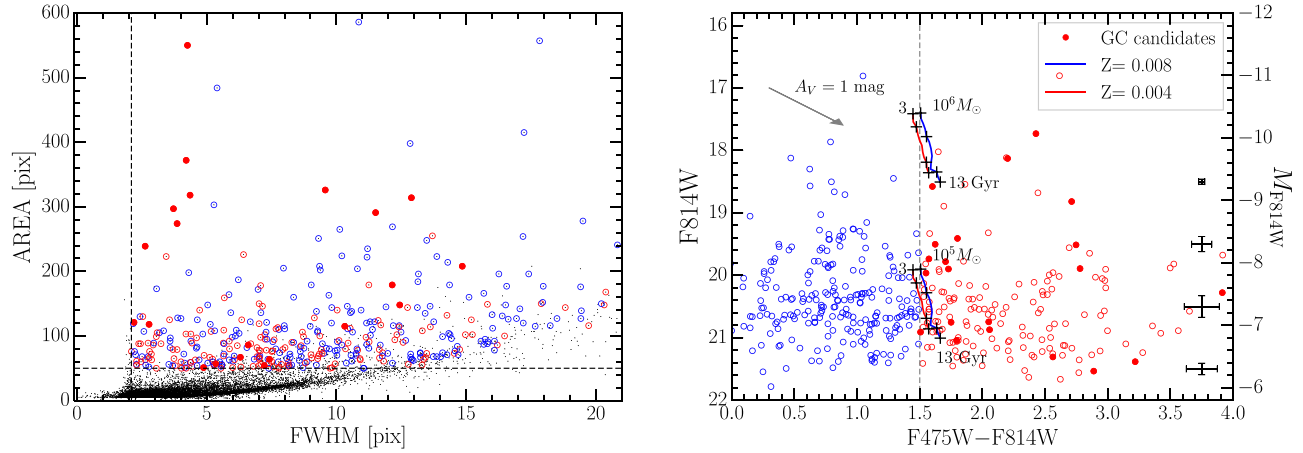

Figure 1. Illustration of selection criteria used in this work to select GC candidates. Left-hand panel: All SExtractor-selected sources (gray dots) plotted along with the clusters candidates (circles) in AREA vs. FWHM plane. Clusters are defined as those objects having FWHM $\geqslant$ 2.1 pix, AREA$>$ 50 pix (dashed lines), F814W $\leqslant$ 22 mag, and ELLIPTICITY $\leqslant$ 0.66 (see text). Right-hand panel: GC candidates (solid red circles) are separated from SSC candidates (blue circles) using the color cut F475W − F814W = 1.5 mag (vertical dashed line). Loci of photometric evolution of clusters between 3 and 13 Gyr using G02 SSPs are shown for two metallicities ($Z = 0.004$ and 0.008) and two cluster masses ($10^5\,M_\odot$ and $10^6\,M_\odot$). The absolute magnitude of clusters is shown along the right-hand axis. The reddening vector corresponding to $A_V = 1$ mag is shown. Open red circles are the red clusters located in the central region of radius = 25″, which are most likely reddened SSCs (see text and Figure 2).

images from the five SDSS filters (*ugriz*) and the three 2MASS bands (JHK_s). The relative isolation of the selected objects allowed us to obtain magnitudes using an aperture with a 2″ radius, except for GCs candidates ID 3 and 37, which were calculated using 1″ radius (see Figure 2).

Table 4 lists the calculated photometry of the 21 GC candidates. Due to the low sensitivity of the 2MASS detectors, photometry of only the brightest clusters was measured.

2.3. Spectroscopic Observations

Spectroscopic observations of a limited sample of GC candidates were obtained using the Multi-Object Spectra (MOS) mode of the Optical System for Imaging and Low-Intermediate-Resolution Integrated Spectroscopy (OSIRIS) instrument on the Gran Telescopio Canarias (GTC). A complete log of observations is shown in Table 5. All observations were carried out using the R1000B grism, covering a spectral range of ∼3700–7500 Å with a spectral resolution of about 5.3 Å and with a sampling of 2.1 Å pixel^{-1}. The spatial scale covered by the spectra is ∼0.″25 pixel^{-1} at the default binning mode (2×2). There were clear skies, seeing was ∼1″ during the two runs. Cirrus clouds were reported only for the 2017A-MOS4 run.

The top panel of Figure 2 displays the GC candidates observed (colored rectangles) with the MOS mode of OSIRIS. Four masks (slits of each mask are indicated with a particular color) were designed to perform the observations in the MOS mode. The slits (colored rectangles) were oriented along the north–south direction, each slit is 1.″2 width. Due to astronomical and instrumental limitations, only 15 GC candidates were spectroscopically observed, with some clusters observed more than once. Each run included bias, flat-fields, calibration lamps, and a standard star (see Table 5).

The data reduction was carried out using the GTCMOS[5] package, an IRAF-based pipeline developed by one of the authors (Y.D. Mayya, see V. M. A. Gomez-Gonzalez et al. 2016 for details). OSIRIS uses two detectors with a small separation along the spatial axis, therefore the first step of the reduction process was to create a mosaic image by joining the images of the two detectors. Subsequently, all the bias frames for each night were combined using the median to obtain a master bias, which was subtracted from all the object frames. The spectra of the comparison lamps were employed to calibrate in wavelength each spectrum, whereas the standard star spectra were used to perform the flux calibration. The task *apall* was used to extract sky-subtracted 1D spectrum of each object. Some of the properties of the extracted spectra, such as the RMS error, signal-to-noise (SNR) of the continuum, and the extraction apertures in units of pixels of 0.25 arcsec, are given in Table 6.

A total of 23 spectra of 15 GC candidates were extracted. All the spectra were corrected for Doppler effect using the IRAF task *dopcor*. At least three absorption features, mainly H and K of CaII, and iron lines, distributed all along the observed wavelength interval were employed to measure the recessional velocity, which is given in column 2 of Table 6. The spectra of these 15 candidates are shown in Figure 3, where we have identified the location of the absorption features typical of old stellar systems such as GCs with vertical gray bars. In two spectra (IDs 124 and 329), most of these features are hardly recognizable due to poor signal-to-noise ratio (SNR), because of which we dropped these candidates from further spectroscopic analysis. Three of our spectroscopic targets turned out to be stars after our GAIA DR3 data analysis (see the next section), leaving us with 10 GC candidates with good quality spectra.

3. The Sample of Confirmed GC Candidates

3.1. Star-GC Discrimination using GAIA Parameters

We find that three of our GC candidates (IDs 3, 5, and 10) were classified as stars by D04 using ground-based NIR photometry. SExtractor and IRAF give us FWHMs for these objects that are significantly greater than the expected value for a point source (FWHM $<$ 2.1 pix) on the HST images. We found that their peak fluxes on the HST images are close to saturation limit, which makes the measured FWHM larger than that expected for a point source. The availability of GAIA DR3

[5] GTCMOS pipeline: https://www.inaoep.mx/~ydm/gtcmos/gtcmos.html

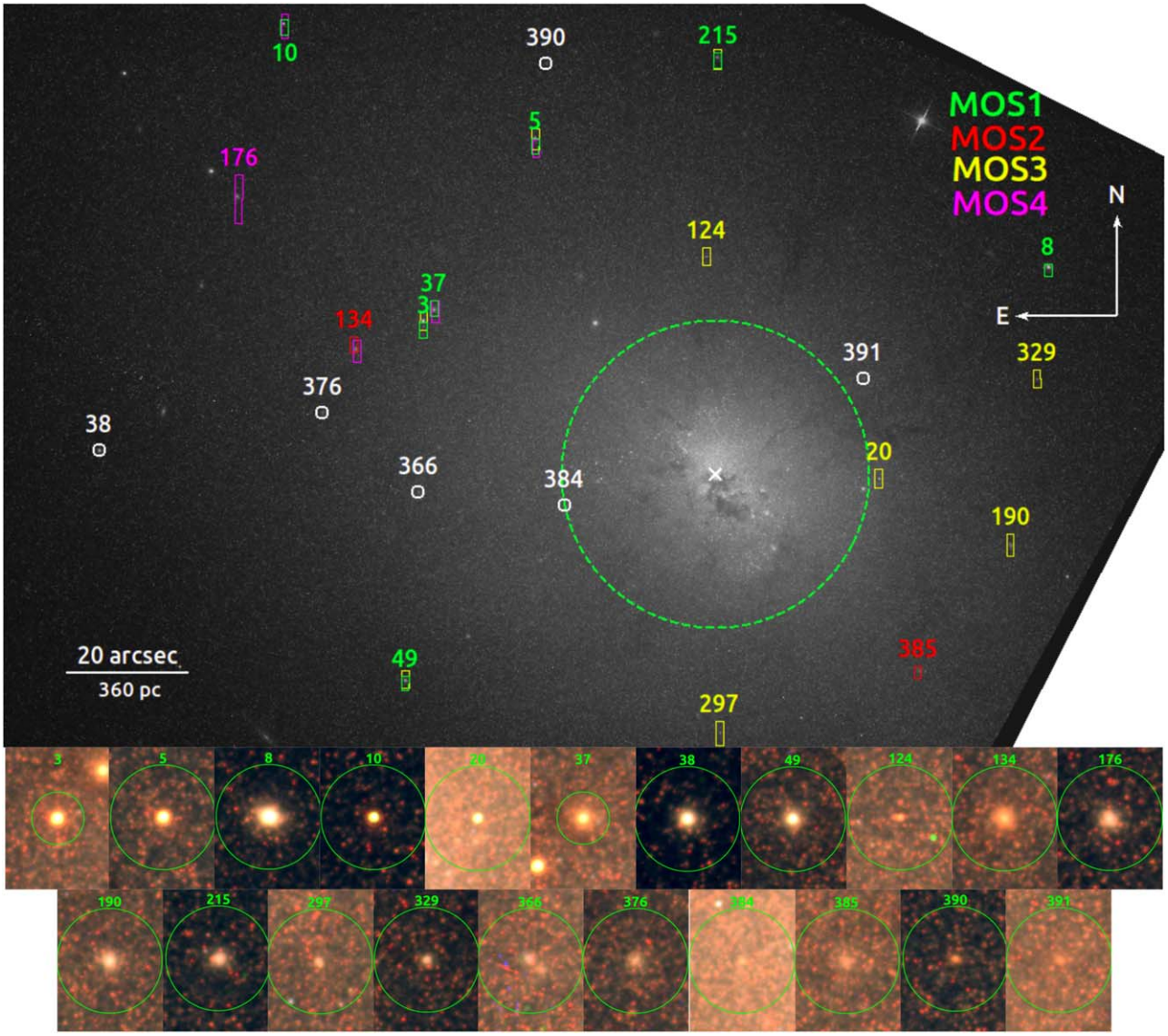

Figure 2. Top panel: GC candidates are displayed on the image of NGC 3077 (F814W band). Objects inside a rectangle were observed with MOS, and the sizes of the rectangles correspond to the sizes of the slitlet, the color indicates the observing run (see the top right-hand corner). GC candidates not observed with MOS are located inside white circles. The central dusty starburst zone is enclosed with a green circle with a radius of 25″. Center at $\alpha = 10^{h}03^{m}19\overset{s}{.}07$ and $\delta = +68°44'02\overset{''}{.}1$ is indicated with white cross. Bottom panels: The RGB (F475W, F606W, and F814W) stamps of the GC candidates are displayed, each circle has a radius of 2″ (36 pc), except ID 3 and 37, both have a radius of 1″ to avoid reciprocal contamination.

data offers a modern method to verify the nature of these three suspected stars, as well as to identify any other Galactic interlopers in our sample. Eight of our GC candidates are bright enough to have a GAIA entry. In Table 7, we give the relevant GAIA parameters for these eight GC candidates. The three suspected stars (IDs 3, 5, and 10) have parallaxes that correspond to distances below ∼2 kpc, confirming them as the Galactic stars.

A. K. Hughes et al. (2021) showed that there are two GAIA parameters that help to identify the Galactic stars in extragalactic GC samples, even when parallax measurements are unreliable. These two additional parameters are the astrometric excess noise (AEN) and the BP/RP (blue photometry/red photometry) excess factor. Extended and marginally extended sources have higher values of these parameters with respect to point sources, with a tendency for fainter objects to have larger values of these parameters. A. K. Hughes et al. (2021) defined the dependence of these parameters with magnitude by curves that discriminate point sources from extragalactic GCs in nearby galaxies. In Figure 4, we show our GC candidates (empty circles) in plots involving these GAIA parameters. The three objects previously noted as stars (IDs 3, 5, and 10) all lie below or very close to the curve in both plots. ID 20 lies marginally below the curve in the AEN plot but lies well above the curve in the BR/RP excess factor plot. This source does not have measurable parallax, and hence we consider it as a GC candidate rather than a Galactic star. The other four objects lie above the curve in both plots, confirming them as marginally resolved extragalactic GCs.

We make use of these GAIA star cluster discriminators to check the possibility that some of the GC candidates of D04 are foreground Galactic stars. We show in Figure 4 all the GC candidates of D04 by black points. Only three objects pass the criteria for extragalactic GCs (marginally resolved objects)—the same two objects that we classified as GC candidates (IDs 8 and 38) and the third object is classified as young SSC (color

Table 3
Parameters of the GC Candidates

ID (1)	R.A. (2)	Decl. (3)	F814W (4)	F475W − F814W (5)	F300W (6)	FWHM (7)	R_G (8)	Obj Type (9)	Confirmation (10)	Other IDs (11)
3*	$10^h03^m27\overset{s}{.}84$	$+68°44'27\overset{''}{.}21$	17.731 ± 0.001	2.427 ± 0.002	23.633 ± 0.441	3.86	949.0	S	GAIA	11(D), 100(N)
5*	$10^h03^m24\overset{s}{.}51$	$+68°44'56\overset{''}{.}81$	18.129 ± 0.001	2.201 ± 0.002	23.392 ± 0.204	3.21	1094.5	S	GAIA	15(D), 107(N)
8	$10^h03^m09\overset{s}{.}17$	$+68°44'35\overset{''}{.}93$	18.578 ± 0.001	1.601 ± 0.002	⋯	4.26	1118.7	GC	Spectra	27(D), 74(N)
10*	$10^h03^m32\overset{s}{.}02$	$+68°45'15\overset{''}{.}56$	18.818 ± 0.001	2.712 ± 0.004	⋯	3.13	1790.4	S	GAIA	8(D), 114(N)
20	$10^h03^m14\overset{s}{.}23$	$+68°44'01\overset{''}{.}53$	19.409 ± 0.005	1.801 ± 0.006	23.773 ± 0.255	2.20	463.5	GC	Spectra	⋯
37	$10^h03^m27\overset{s}{.}53$	$+68°44'29\overset{''}{.}03$	19.513 ± 0.004	2.747 ± 0.010	24.348 ± 0.696	4.21	938.2	IAC	SED	12(D), 101(N)
38	$10^h03^m37\overset{s}{.}52$	$+68°44'06\overset{''}{.}15$	19.503 ± 0.003	1.623 ± 0.004	⋯	4.36	1768.1	GC	SED	1(D), 104(N)
49	$10^h03^m28\overset{s}{.}38$	$+68°43'28\overset{''}{.}72$	19.737 ± 0.004	1.573 ± 0.005	22.909 ± 0.184	4.12	1068.0	IAC	Spectra	48(N)
124†	$10^h03^m19\overset{s}{.}38$	$+68°44'37\overset{''}{.}62$	20.278 ± 0.009	3.914 ± 0.043	⋯	3.15	625.8	Blended	Visual	⋯
134	$10^h03^m29\overset{s}{.}86$	$+68°44'22\overset{''}{.}55$	19.892 ± 0.011	2.779 ± 0.014	23.809 ± 0.725	7.66	1094.2	IAC	Spectra	9(D), 102(N)
176	$10^h03^m33\overset{s}{.}41$	$+68°44'47\overset{''}{.}47$	19.781 ± 0.015	1.706 ± 0.009	23.341 ± 0.886	7.02	1587.3	IAC	Spectra	111(N)
190	$10^h03^m10\overset{s}{.}30$	$+68°43'50\overset{''}{.}68$	19.964 ± 0.019	1.550 ± 0.010	⋯	7.11	863.7	IAC	Spectra	⋯
215	$10^h03^m19\overset{s}{.}06$	$+68°45'10\overset{''}{.}05$	19.899 ± 0.015	1.729 ± 0.009	⋯	6.60	1195.8	IAC	Spectra	⋯
297	$10^h03^m18\overset{s}{.}97$	$+68°43'20\overset{''}{.}23$	20.871 ± 0.022	2.057 ± 0.020	⋯	5.35	736.9	IAC	SED	⋯
329	$10^h03^m09\overset{s}{.}51$	$+68°44'17\overset{''}{.}72$	21.042 ± 0.015	1.794 ± 0.014	⋯	4.23	955.8	IAC	SED	⋯
366	$10^h03^m27\overset{s}{.}99$	$+68°43'59\overset{''}{.}31$	20.910 ± 0.050	1.506 ± 0.026	⋯	6.21	855.8	IAC	SED	88(N)
376	$10^h03^m30\overset{s}{.}85$	$+68°44'12\overset{''}{.}28$	20.752 ± 0.039	1.750 ± 0.021	24.010 ± 1.389	6.91	1142.3	IAC	SED	97(N)
384	$10^h03^m23\overset{s}{.}63$	$+68°43'57\overset{''}{.}11$	21.308 ± 0.056	2.562 ± 0.064	⋯	4.25	445.4	IAC	SED	⋯
385	$10^h03^m13\overset{s}{.}03$	$+68°43'30\overset{''}{.}28$	20.745 ± 0.046	2.050 ± 0.027	⋯	7.24	805.4	IAC	Spectra	20(N)
390	$10^h03^m24\overset{s}{.}16$	$+68°45'09\overset{''}{.}00$	21.534 ± 0.018	2.888 ± 0.047	⋯	3.73	1274.0	IAC	SED	⋯
391	$10^h03^m14\overset{s}{.}71$	$+68°44'17\overset{''}{.}82$	21.383 ± 0.028	3.219 ± 0.070	⋯	5.44	501.1	IAC	SED	⋯

Note. (1): Identifier: ID numbers followed by a symbol are rejected objects either because they are identified as bright foreground stars ("*") or blended stars (†; see Section 3); (2)–(3) coordinates in the GAIA system (J2000); (4)–(6) magnitudes and color in VEGAMAG system; (7) FWHM in (pix) from F814W HST/ACS; (8) galactocentric radius in (pc) (center at $\alpha = 10^h03^m19\overset{s}{.}07$ and $\delta = +68°44'02\overset{''}{.}1$); (9) object type: GC, S, and IAC for GC, star, and intermediate-age cluster, respectively; (10) confirmation of object type (see text); (11) other IDs: (D) for T. J. Davidge (2004) and (N) for P. Notni et al. (2004).

Table 4
Multiband Photometry of GC Candidates

ID	i	H	$u-i$	$g-i$	$r-i$	$i-z$	$i-K_s$	$H-K_s$	$J-H$
(1)	(2)	(3)	(4)	(5)	(6)	(7)	(8)	(9)	(10)
3*	17.591 ± 0.027	15.650 ± 0.094	3.859 ± 0.370^{u}	2.709 ± 0.083	0.972 ± 0.044	0.610 ± 0.037	1.686 ± 0.244	-0.255 ± 0.261	0.668 ± 0.156
5*	17.957 ± 0.028	16.570 ± 0.101	3.207 ± 0.353^{u}	2.507 ± 0.078	0.837 ± 0.046	0.536 ± 0.052	0.794 ± 0.283	-0.593 ± 0.300	0.837 ± 0.149
8	18.373 ± 0.034	17.142 ± 0.155	2.058 ± 0.199	1.444 ± 0.056	0.459 ± 0.048	0.493 ± 0.069	2.052 ± 0.134	0.821 ± 0.202	1.148 ± 0.281
10*	19.003 ± 0.049	17.287 ± 0.184	2.161 ± 0.355^{u}	2.588 ± 0.136	0.943 ± 0.081	0.708 ± 0.096	1.664 ± 0.248	-0.052 ± 0.305	0.872 ± 0.263
20	17.525 ± 0.100	16.036 ± 0.433	2.210 ± 0.208	1.768 ± 0.126	0.466 ± 0.127	0.262 ± 0.221	1.842 ± 0.275	0.353 ± 0.503	0.760 ± 0.587
37	19.102 ± 0.075	16.472 ± 0.192	2.348 ± 0.377^{u}	2.744 ± 0.245	0.883 ± 0.116	0.616 ± 0.110	2.524 ± 0.378^{K}	-0.106 ± 0.417	0.330 ± 0.249
38	19.338 ± 0.062	⋯	1.725 ± 0.363	1.474 ± 0.099	0.429 ± 0.086	0.353 ± 0.161	1.760 ± 0.357^{K}	⋯	⋯
49	19.589 ± 0.111	⋯	1.575 ± 0.369^{u}	1.236 ± 0.147	0.280 ± 0.139	0.385 ± 0.242	2.011 ± 0.369^{K}	⋯	⋯
124†	20.132 ± 0.231	⋯	1.032 ± 0.421^{u}	2.367 ± 0.569	1.085 ± 0.424	0.376 ± 0.462	2.554 ± 0.421^{K}	⋯	⋯
134	19.417 ± 0.097	⋯	1.747 ± 0.365^{u}	2.470 ± 0.242	0.709 ± 0.145	0.675 ± 0.173	1.839 ± 0.365^{K}	⋯	⋯
176	19.758 ± 0.098	⋯	1.406 ± 0.365^{u}	1.403 ± 0.143	0.537 ± 0.134	0.358 ± 0.260	2.180 ± 0.365^{K}	⋯	⋯
190	19.830 ± 0.162	⋯	1.328 ± 0.414	1.160 ± 0.206	0.427 ± 0.216	0.736 ± 0.269	2.252 ± 0.387^{K}	⋯	⋯
215	20.290 ± 0.161	⋯	0.874 ± 0.387^{u}	1.387 ± 0.222	0.989 ± 0.267	0.553 ± 0.358	2.712 ± 0.387^{K}	⋯	⋯
297	21.685 ± 0.351	⋯	-0.521 ± 0.497^{u}	0.929 ± 0.727	0.803 ± 0.505	1.677 ± 0.487	4.107 ± 0.497^{K}	⋯	⋯
329	20.517 ± 0.215	⋯	0.647 ± 0.412^{u}	2.586 ± 0.582	1.386 ± 0.501	0.854 ± 0.359	2.939 ± 0.412^{K}	⋯	⋯
366	19.909 ± 0.223	⋯	1.255 ± 0.417^{u}	0.692 ± 0.250	0.218 ± 0.276	0.522 ± 0.358	2.331 ± 0.417^{K}	⋯	⋯
376	20.519 ± 0.248	⋯	0.645 ± 0.431^{u}	1.762 ± 0.404	0.587 ± 0.347	0.496 ± 0.419^{z}	2.941 ± 0.431^{K}	⋯	⋯
384	19.314 ± 0.173	⋯	1.850 ± 0.392^{u}	0.788 ± 0.219	0.260 ± 0.230	-0.694 ± 0.380	1.736 ± 0.392^{K}	⋯	⋯
385	20.036 ± 0.184	⋯	1.128 ± 0.397^{u}	1.552 ± 0.291	0.632 ± 0.268	0.618 ± 0.336	2.458 ± 0.397^{K}	⋯	⋯
390	21.468 ± 0.465	⋯	-0.304 ± 0.583^{u}	1.926 ± 0.605	1.022 ± 0.796	1.460 ± 0.575	3.890 ± 0.583^{K}	⋯	⋯
391	19.354 ± 0.140	⋯	1.810 ± 0.379^{u}	1.417 ± 0.214	0.591 ± 0.215	-0.180 ± 0.414	1.776 ± 0.379^{K}	⋯	⋯

Note. (2)–(3) Magnitudes in VEGAMAG system, (4)–(10) colors in VEGAMAG system. Most of the clusters are very faint, therefore in some bands their magnitudes are given by an upper limit (denoted with a super index). We did not write a color value if both magnitudes are upper limits.

Table 5
Log of the Spectroscopic Observations Using GTC/OSIRIS

Run (1)	PI (2)	Date (3)	SW (4)	Exp. Time (5)	AM (6)	Seeing (7)	Night (8)	STD (9)	Obj (10)
2015B-MOS1	L. H. Rodríguez-Merino	2015-12-17	1.2	3 × 1300	1.34	1.0	G	G191-B2B	7
2015B-MOS2	L. H. Rodríguez-Merino	2015-12-17	1.2	3 × 1300	1.30	0.9	G	G191-B2B	2
2017A-MOS3	L. H. Rodríguez-Merino	2017-04-22	1.2	3 × 1500	1.32	1.1	D	HILT600	9
2017A-MOS4	L. H. Rodríguez-Merino	2017-04-02	1.2	3 × 1500	1.30	0.9	D	HILT600	5

Note. (1) ID of the Run, (2) principal investigator, (3) observational date, (4) slit-width (arcsec), (5) exposure time (number of exposures × integration time in seconds), (6) mean air mass of the three exposures, (7) seeing (arcsec), (8) type of night (G = gray or D = dark), (9) standard star, (10) number of objects in each run.

Table 6
Characteristics of the Spectra Obtained with GTC

ID (1)	Velocity (2)	rms (3)	SNR (4)	Obj Type (5)	Runs (6)	Ap. Size (7)
3*	−163 ± 26	1.2	17	2	MOS 1,3	3
5*	−79 ± 8	1.0	21	2	MOS 1,3,4	3
8	−78 ± 38	1.5	19	1	MOS 1	4
10*	−85 ± 35	1.4	8	2	MOS 1,4	4
20	−57 ± 29	1.4	14	1	MOS 3	4
37	−90 ± 30	1.4	12	3	MOS 1,4	4
49	120 ± 10	2.5	12	3	MOS 1,3	4
124†	68 ± 12	0.9	9	3	MOS 3	4
134	46 ± 31	1.7	12	3	MOS 2,4	4
176	−164 ± 42	1.2	6	3	MOS 4	4
190	71 ± 23	1.2	10	3	MOS 3	4
215	−38 ± 36	1.8	9	3	MOS 1,3	5
297	−129 ± 34	1.4	6	3	MOS 3	4
329†	−51 ± 28	0.9	8	3	MOS 3	4
385	−84 ± 32	1.3	17	3	MOS 2	4

Note. (1) Identification numbers. A superscript "*" or "†" signs imply they are stars, or the spectra have insufficient quality to measure spectral indices, respectively, (2) Observed recessional velocity (measuring mainly H and K of CaII, and iron lines) in (km s^{-1}), (3)–(4) root mean square (rms) of the continuum ($\times 10^{-18}$ erg s^{-1} cm^{-2} Å^{-1}) and signal-to-noise ratio (SNR) of the spectrum, both measured at 4150 Å in a 100 Å window. In case a GC candidate has been observed two or more times, we employed the spectrum with the highest SNR (see Section 2.3), (5) same as defined in column 8 of Table 3, (6) same as defined in column 1 of Table 5, (7) aperture size for extraction in (pix).

F475W − F814W < 1.5 mag, see Section 2.1) by us. The rest of the objects have FWHM on the HST images consistent with them being stars. The implications of this will be discussed in Section 5.2.

3.2. Star-GC Discrimination using Color–Color Diagram

The color–color diagram $(i - K_s)_0$ versus $(u - i)_0$ has been established to be a useful diagram to discriminate the Galactic interlopers from genuine GCs (R. P. Muñoz et al. 2014; R. A. González-López lira et al. 2017). The resulting plot is shown in Figure 5. Some of our candidates are not detected at either the shortest (u) or/and the longest (K_s) bands, in which case the observed colors are either bluer or redder limits, respectively. A short arrow is shown when it is undetected in only one of the u or K_s bands, whereas inverted red triangles are put when it is not detected in both filters. The reddening vector for $A_V = 1$ mag using the C89 extinction curve is shown by the arrow. The plotted colors have been corrected for the Galactic reddening of $E(B - V) = 0.07$ mag (D. J. Schlegel et al. 1998) but not for any internal reddening in the host galaxy. We also show as the green area the expected location of GCs, modeled as old SSPs between $Z = 0.001$ and 0.02 (G02) and the locus of the zero age main sequence (ZAMS), where the majority of the Galactic field stars lie. The plotted ZAMS locus is taken from the theoretical stellar evolutionary code PARSEC[6] at the same four metallicities (A. Bressan et al. 2012).

Objects in the diagram with colors that are consistent with the colors of the green area will be identified as GCs, whereas those close to the ZAMS locus are likely to be the Galactic stars. Except the three candidates identified as stars (IDs 3, 5, and 10), all the rest are consistent as GCs after taking into account the detection-limit arrows. Objects that are undetected in the u and K bands fall along a diagonal with their nondetections consistent with the colors expected for GCs.

3.3. Final List of GC Candidates

Finally, a careful visual inspection of each GC candidate allowed us to reject a fourth object, ID 124 because it shows morphological signatures of being composed by two point sources. In summary, we removed four objects from the initial list to get a total sample of 17 objects that have colors and sizes suggesting they are genuine GC candidates.

We could obtain radial velocity measurements from our spectroscopic observations for 11 of these objects, which are plotted against the galactocentric radius R_G in Figure 6. The recessional velocity of galaxy is shown by the dashed line (see Table 1). All the GC candidates have values within 200 km s^{-1} of the recessional velocities.

4. Metallicity and Age from Spectro-photometric Analysis

The observed spectrum of each cluster was used to determine two of the most important physical parameters of a stellar population: age and metallicity. Two methods are in common use to obtain these two quantities from spectroscopic data: (1) simultaneous measurement of age and metallicity by fitting the entire spectrum with a model spectrum, and (2) use of age-insensitive spectral features among the Lick indices to obtain metallicity and then use the entire spectrum to get the best determination of the age. The former technique is greatly in use to analyze large spectral databases such as SDSS spectra (e.g., E. Pérez et al. 2013), whereas the latter technique gives more reliable results for individual objects, especially when the SNR is ∼20 or less (e.g., S. S. Larsen et al. 2001; Y. D. Mayya et al. 2013 hereafter, M3). We used the latter method in this study for analyzing the spectroscopic data of our GC candidates.

For the GC candidates with no observed spectrum, we obtained ages and extinctions by SED-fitting to the multiband photometry with SSP models (Section 4.3).

[6] http://stev.oapd.inaf.it/cgi-bin/cmd

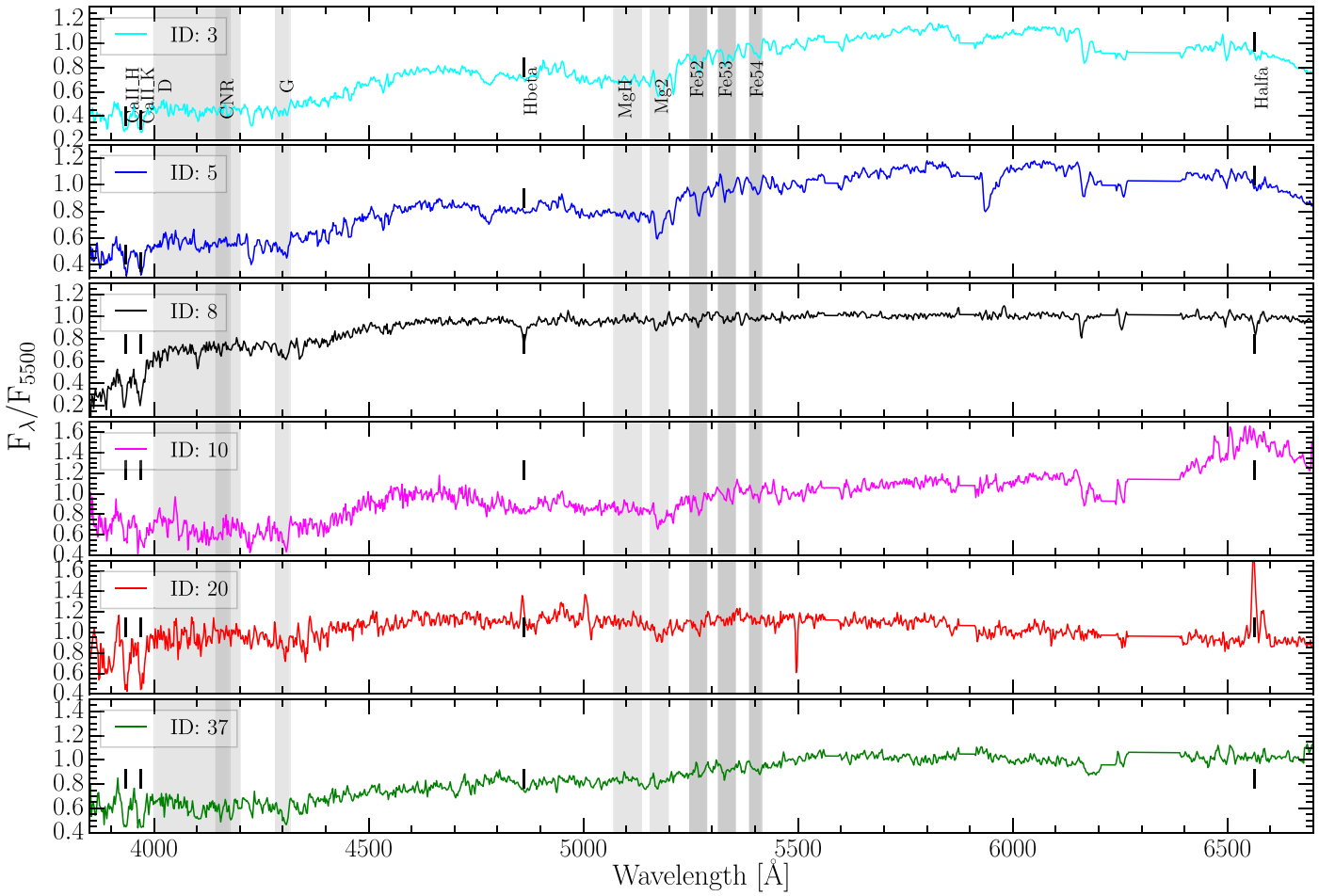

Figure 3. GTC/OSIRIS-MOS spectra of all observed GC candidates, the three foreground stars are included (IDs 3, 5, and 10, see Section 3). The fluxes are corrected for the Galactic reddening and Doppler effect. To facilitate visualization, the fluxes have been normalized to F_{5500} value. The shaded areas indicate regions where spectral indices (labels in the top panel) were defined by D. Burstein et al. (1984), J. P. Brodie & J. P. Huchra (1990), and S. C. Trager et al. (1998).

4.1. Metallicity Determination

Absorption lines of cool stars allow the determination of stellar metallic abundances and ages. Among all the absorption lines, the iron lines Fe5270, Fe5335, and Fe5406 (Fe52, Fe53, and Fe54, respectively) are sensitive primarily to metallicity for stellar systems older than ∼3 Gyr (M13; L. Lomelí-Núñez et al. 2024) independent of their ages. We used this property of Fe indices to obtain the metallicity of our GC candidates. These three spectroscopic indices were defined by D. Burstein et al. (1984), J. P. Brodie & J. P. Huchra (1990), and S. C. Trager et al. (1998), and were empirically calibrated as a function of the metallicity, [Fe/H], using the spectra of Galactic GCs provided by R. P. Schiavon et al. (2005). For each index, a second order equation was fitted to the relation of the index against the metallicity (see Figure 4 in M13 and also L. Lomelí-Núñez et al. 2024).

Each spectral index gives us an independent determination of the iron abundance. In some cases, the extracted spectrum, with poor SNR, does not behave very well near the spectral features showing small jumps or is dominated by noise, making the index unusable. Hence, the metallicity of each cluster was obtained as the mean of the three values, weighted by the inverse of their variance. Figure 7 shows the metallicity of the GC candidates determined as a function of the measured indices Fe52, Fe53, and Fe54. Each panel displays the results obtained with one index. We conducted a Monte Carlo simulation to estimate the errors in the metallicity. For each observed spectrum, we generated one thousand simulated observations by randomly adding noise with a rms value calculated for each index interval. Equations (1) and (2) of J. P. Brodie & J. P. Huchra (1990) were employed to measure the spectral indices of each simulated spectrum. The metallicity estimates [Fe/H] along with their errors are given in Table 8.

Additionally, we determined the [α/Fe] ratios (alpha element enrichment) of the GC candidates using the relation between Mg $b/\langle$Fe$\rangle$ and [α/Fe] (where $\langle$Fe$\rangle = 0.5 \times$ (Fe5270 + Fe5335) defined by D. Thomas et al. (2003). For this purpose, we have degraded the observed spectra to mimic the resolution of the Lick/IDS system (see G. Worthey et al. 1994), and we employed the definitions according to the Lick/IDS system to measure the Mg*b*, Fe5270, and Fe5335 indices. A new Monte Carlo simulation was applied to calculate the uncertainties of these indices.

We have parameterized the Mg$b/\langle$Fe$\rangle$ − [α/Fe] (dark area of Figure 4 in D. Thomas et al. 2003) relation with the second order equation,

$$[\alpha/\mathrm{Fe}] = \frac{-1 + \sqrt{\mathrm{Mg}b/\langle\mathrm{Fe}\rangle - 0.2}}{0.75}, \quad (1)$$

which is applicable for Mg$b/\langle$Fe$\rangle > 1$ and [α/Fe] > -0.05 . We could employ this equation to determine the alpha element enhancement in six clusters for which the measured Mg$b/\langle$Fe$\rangle > 1$.

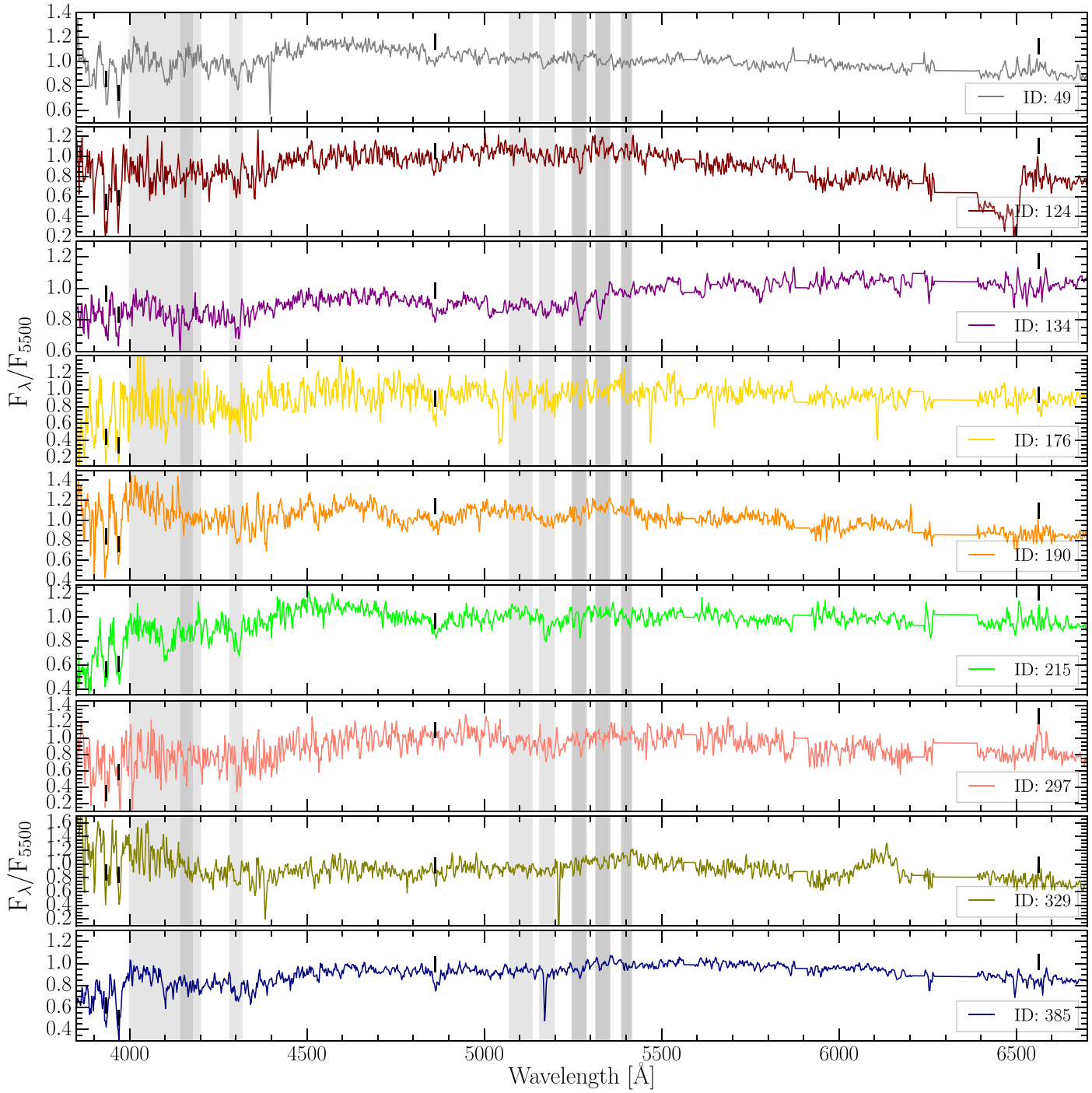

Figure 3. (Continued.)

Table 9 shows the values of F52, Fe53, Mg *b* indices, and Mg $b/\langle \mathrm{Fe} \rangle$ and $[\alpha/\mathrm{Fe}]$ ratios.

4.2. Spectroscopic Age and Reddening Determination

Once the chemical abundances of the clusters were determined, we proceeded to calculate the age and reddening of the GC candidates. The first step to deredden the observed spectra was to correct them for the Galactic extinction using $A_V = 0.21$ mag (D. J. Schlegel et al. 1998), and the extinction curve established by C89 with $R_V = 3.1$. The best-fitting method was employed to determine the age and the local reddening, $E(B-V)$, of the GC candidates. The software tool known as Analyzer of Spectra for Age Determination (ASAD; R. S. Asa'd 2014) was used to determine the log(Age) and $E(B-V)$ values for the observed spectra.

The ASAD code is designed to determine the age and reddening of an observed spectrum by seeking the best-fit match through a comparison of the observed spectrum with a set of SSP models (spectra). The process of identifying the best

Table 7
Parameters of the GC Candidates from GAIA DR3

ID (1)	ID_G (2)	Parallax (3)	pmRA (4)	pmDec (5)	G (6)	AEN (7)	BP/RP (8)
3*	0528	1.397 ± 0.149	10.56 ± 0.15	-7.34 ± 0.13	18.56	0.00	1.34
5*	5248	0.877 ± 0.174	2.15 ± 0.17	4.27 ± 0.15	18.79	0.04	1.70
8	6912	...	-2.10 ± 0.99	-0.21 ± 0.87	20.02	7.03	3.24
10*	7408	0.495 ± 0.381	0.30 ± 0.38	-4.50 ± 0.33	19.82	1.27	1.49
20	5008	...	0.92 ± 0.60	-8.95 ± 0.62	20.23	2.77	2.85
37	4528	...	...	...	21.27	19.38	4.23
38	1968	...	...	...	20.96	16.04	3.25
49	3824	...	...	...	21.01	12.91	3.30

Note. (2) Last four numbers of GAIA ID, (3) parallax (π) in (mas), (4)–(5) proper motion of R.A. and decl. in (mas yr^{-1}), (6) G-band magnitude in (mag), (7) astrometric excess noise in (mas), (8) BP/RP excess factor.

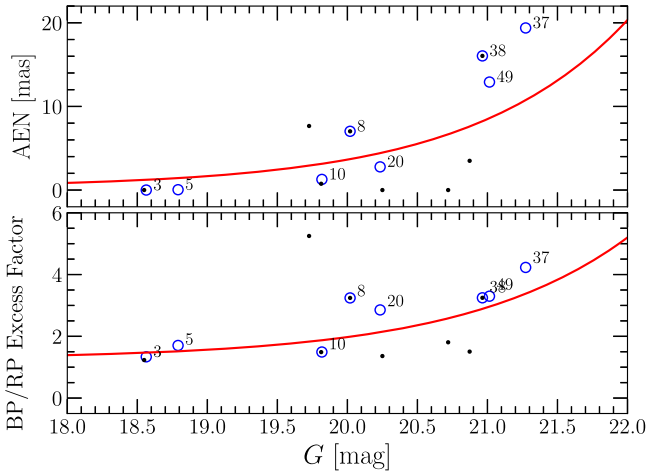

Figure 4. Astrometric and photometric data provided by GAIA is employed to confirm GC candidates (blue circles). Two diagrams, AEN vs. G-band magnitude and blue photometry/red photometry (BP/RP) vs. G-band magnitude, are used to distinguish between foreground stars from extragalatic extended sources. GC candidates of D04 with entry in GAIA list are represented as black points (see text). Foreground stars lay under the red line (see A. K. Hughes et al. 2021).

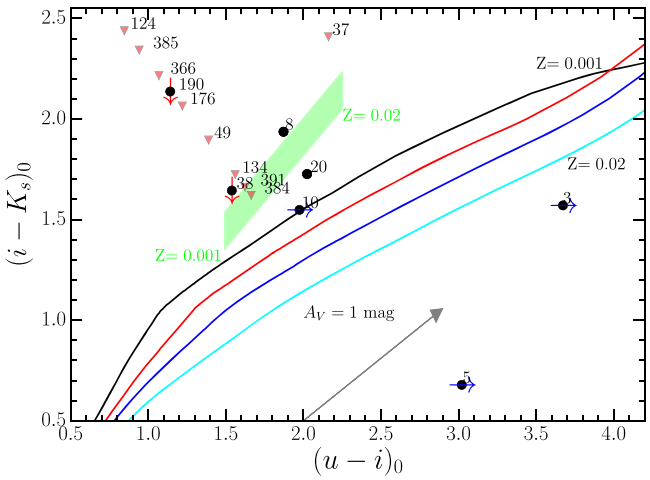

Figure 5. Color–color diagram $(i - K_s)_0$ vs. $(u - i)_0$ comparing the colors of the GC candidates (circles and triangles). Many candidate GCs are undetected in either the u-band (right arrows) or the K_s-band (down arrows) or in both these (inverted triangles). Colors obtained with SSP models span over this diagram (green area), they cover the age interval from 8 to 13 Gyr and four metallicities: $Z = 0.001$, 0.004, 0.008, and 0.02. Four theoretical ZAMS models are included, which are indicated with colored continuous lines and have the same metallicities as SSPs. The extinction vector corresponds to $A_V = 1$ mag.

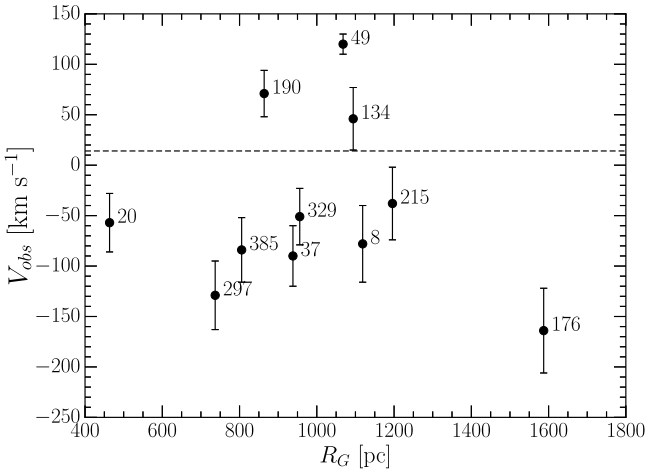

Figure 6. Radial velocities of the confirmed GC candidates against galactatocentric radius (R_G). The velocity of the galaxy is represented with a dashed line (see Table 1).

fit is accomplished by minimizing the χ^2, which is defined as follows (R. S. Asa'd 2014):

$$\chi^2 = \sum_{\lambda=\lambda_{\min(\text{Å})}}^{\lambda_{\max(\text{Å})}} \left(\frac{(\text{OF})_\lambda - (\text{MF})_\lambda}{(\text{OF})_\lambda} \right)^2, \quad (2)$$

where OF and MF are the observed and the model flux (normalized at 5500 Å), respectively.

The synthesis of the SSP models is based on the work by A. Vazdekis et al. (2010). These models were developed using the Kroupa initial mass function (IMF, P. Kroupa 2001), the evolutionary tracks known as "*Padova+00*" tracks by L. Girardi et al. (2000), and the Medium-resolution INT Library of Empirical Spectra (MILES) library of observed spectra provided by P. Sanchez-Blazquez et al. (2006). The SSP models were acquired from the MILES web page[7] and subsequently custom-built to the specific requirements of our spectroscopic data analysis.

Based on the results previously calculated, we conducted the analysis of each spectrum by utilizing reddened models with chemical enrichment that closely approximates the already determined metallicity. Precisely, we employed SSP models with metallicities of [Fe/H] = −1.31 and −0.71 dex, and ages ranging from log(Age) = 7.8–10.25 yr in increments of 0.05 dex, the

[7] http://research.iac.es/proyecto/miles/pages/webtools/tune-ssp-models.php

Table 8
Physical Parameters of the Clusters Obtained with the Analysis of the Spectroscopic Data

ID (1)	$[Fe/H]_{Fe52}$ (2)	$[Fe/H]_{Fe53}$ (3)	$[Fe/H]_{Fe54}$ (4)	$[Fe/H]_{mean}$ (5)	$[Fe/H]_{SSP}$ (6)	log(Age) (7)	$E(B-V)$ (8)	A_V (9)	χ^2_{min} (10)
8	-1.34 ± 0.25	-0.79 ± 0.20	-1.27 ± 0.15	-1.13 ± 0.11	-1.31	10.18 ± 0.05	0.18 ± 0.01	0.56 ± 0.03	2.93
20	-0.91 ± 0.28	-0.94 ± 0.21	-1.35 ± 0.24	-1.06 ± 0.14	-1.31	10.12 ± 0.10	0.04 ± 0.04	0.12 ± 0.12	3.80
37	...	-0.61 ± 0.21	-0.84 ± 0.25	-0.71 ± 0.16	-0.71	...	...	...	...
49	-1.40 ± 0.28	-1.19 ± 0.32	-1.77 ± 0.26	-1.49 ± 0.16	-1.31	9.62 ± 0.10	0.00 ± 0.01	0.00 ± 0.03	4.65
134	...	...	...	-0.71	-0.71	9.39 ± 0.20	0.12 ± 0.05	0.37 ± 0.15	10.85
176	...	...	...	-0.71	-0.71	9.62 ± 0.20	0.00 ± 0.01	0.00 ± 0.03	23.48
190	-1.23 ± 0.33	-1.60 ± 0.42	-1.23 ± 0.35	-1.32 ± 0.21	-1.31	9.48 ± 0.20	0.00 ± 0.01	0.00 ± 0.03	10.56
215	-0.69 ± 0.31	-1.01 ± 0.23	-0.77 ± 0.28	-0.86 ± 0.16	-0.71	9.47 ± 0.10	0.00 ± 0.01	0.00 ± 0.03	6.53
297	-0.78 ± 0.43	-0.65 ± 0.29	...	-0.69 ± 0.24	-0.71	...	...	...	...
385	-0.73 ± 0.21	-0.89 ± 0.24	-0.92 ± 0.18	-0.85 ± 0.12	-0.71	9.64 ± 0.10	0.02 ± 0.01	0.62 ± 0.03	7.88

Note. (2) Metallicity calculated using F52 index, (3) metallicity calculated using F53 index, (4) metallicity calculated using F54 index, (5) weighted mean metallicity (metallicity of IDs 134 and 174 was fixed), (6) metallicity of the model employed to determine log(Age) and reddening ($E(B-V)$), (7) log(Age) of the best-fitted model, (8) $E(B-V)$ of best-fitted model, (9) extinction of the best-fitted model ($R_V = 3.1$), (10) minimal χ^2 obtained with the best-fitted model. IDs 37 and 297 did not provide reliable estimates.

Table 9
α-enhancement of the Clusters

ID (1)	Fe52 (2)	Fe53 (3)	Mgb (4)	Mg$b/\langle$Fe$\rangle$ (5)	$[\alpha/$ Fe] (6)
8	1.16 ± 0.19	1.40 ± 0.15	1.58 ± 0.19	1.24 ± 0.19	0.03 ± 0.12
20	1.49 ± 0.28	1.04 ± 0.17	2.02 ± 0.25	1.60 ± 0.28	0.24 ± 0.16
37	...	1.56 ± 0.24	0.37 ± 0.30	...	...
49	1.17 ± 0.23	1.29 ± 0.13	1.54 ± 0.19	1.25 ± 0.21	0.03 ± 0.14
134	2.00 ± 0.58	2.79 ± 0.47	0.94 ± 0.26	0.39 ± 0.13	...
176	1.05 ± 0.62	1.65 ± 0.35	0.61 ± 0.40	0.45 ± 0.32	...
190	0.97 ± 0.26	0.99 ± 0.16	1.12 ± 0.10	1.14 ± 0.21	-0.04 ± 0.14
215	1.78 ± 0.31	0.75 ± 0.12	2.52 ± 0.40	1.99 ± 0.41	0.45 ± 0.21
297	1.83 ± 0.52	1.54 ± 0.31	1.40 ± 0.43	0.83 ± 0.29	...
385	1.72 ± 0.25	1.19 ± 0.21	2.88 ± 0.79	1.99 ± 0.59	0.45 ± 0.29

Note. (2)–(4) Indices Fe52, Fe53, and Mgb, (5) Ratio Mg $b/<$Fe$>$, (6) α-enhancement from D. Thomas et al. (2003; see text).

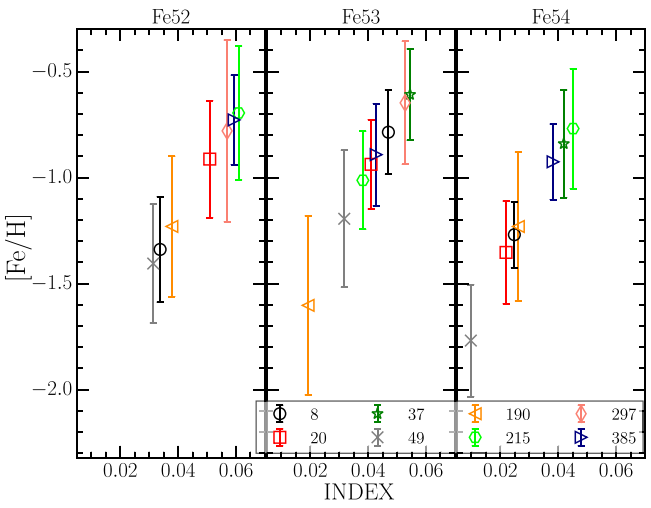

Figure 7. Three spectral indices (Fe52, Fe53, and Fe54) were employed to measure the metallicity (see text) of the GC candidates (see box). The mean metallicity is shown in Table 8.

reddening of spectra spans over a range of $E(B-V) = 0$–1 mag, in steps of 0.01 mag.

To ensure the robustness and accuracy of the fitting process, we narrowed the analysis to a specific wavelength range, which extended from 3900 to 6700 Å (up to 5600 Å for ID 20). The uncertainties associated with the ages and reddening values calculated were determined with a series of Monte Carlo simulations. Similarly to previous Monte Carlo simulations, each observed spectrum produces one thousand simulated "observed" spectra. We determined the age and reddening for each mock spectrum.

Values of log(Age) and extinction obtained for the clusters are presented in Table 8 and illustrated in Figure 8. This figure illustrates both the observed spectra (black line) and their corresponding best-fitted models (red line). The boxes in each panel display the values of the best-fit log(Age) and reddening. The best-fitted model reproduces pretty well several features of the observed spectrum (see upper part of each panel). Residuals are shown in the lower part of each panel, which are less than 10% in the majority of cases.

Based on this spectral analysis, objects IDs 8 and 20 are identified as classical GCs with ages exceeding 13 Gyr and poor in metals, while the rest are determined to be considerably younger, with ages between 3 and 5 Gyr and metal-rich ($[Fe/H] \sim -0.71$ dex). We refer to the latter group of clusters as the intermediate-age clusters (IACs). The detailed implications and discussions regarding these classical GCs and IACs will be explored and presented in Section 5.

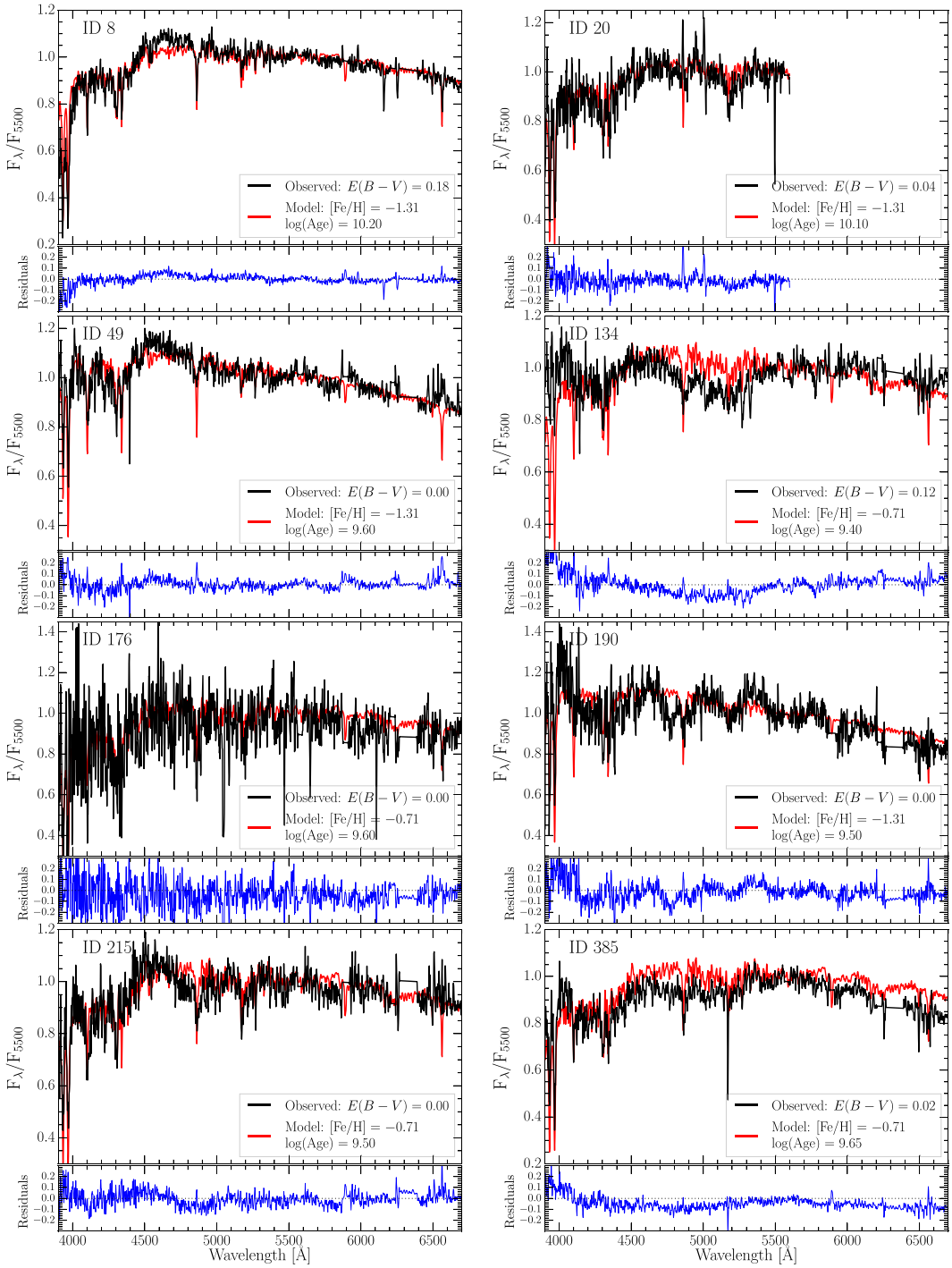

Figure 8. The panels display the results obtained with the best-fitting method (see box) using ASAD code. Each result is described with two panels: the upper panel shows the observed spectrum and best-fitting model (fluxes are normalized to F_{5500}), while the lower panel shows the residual spectrum, given by Fobs − Fmdl. Clusters IDs 8 and 20 are identified as classical GCs (see text), while the rest are estimated to be younger, with ages $\lesssim$4 Gyr.

4.3. Physical Parameters from SED-fitting

We could only obtain age, metallicity, and extinction for 10 of the 17 GC candidates. The rest of the objects are not observed spectroscopically, or the observed spectra are of bad quality. We used the popular technique of SED-fitting approach using the multiband photometry ranging from 3000 Å to 2.2 μm in filters listed in Table 2. The use of this range of colors, especially the $g - K_s$ color, is particularly useful to break the age-metallicity degeneracy for old populations, as illustrated in Figure 7 of M13. Thus, we obtain the age, metallicity, and extinction for all GC candidates. The availability of independent determination of these quantities using spectroscopy for 10 of the objects allows us to authenticate the determined values.

We constructed a theoretical grid of colors employing SSP models calculated by G02 using the Kroupa IMF. The ages varied from 1 Myr to 12.6 Gyr at logarithmic steps of 0.05 dex at the $Z = 0.02$ and 0.008. We increased the starting point of the age grid to 4 and 5.6 Gyr at $Z = 0.004$ and 0.001,

respectively, given that we do not expect young metal-poor clusters in our sample. The grid incorporates these four metallicities. To simulate the effects of internal extinction, the synthetic colors were reddened using the C89 extinction curve. We varied the A_V value from 0.0 to 3.0 mag in steps of 0.01 mag. The number of these synthetic colors is ∼3000.

The age, metallicity, and extinction of each star cluster are determined using a χ^2 minimization approach. The χ^2 value is defined as:

$$\chi^2 = \sum_i \omega_i \frac{(\mathrm{color}_i^{\mathrm{obs}} - \mathrm{color}_i^{\mathrm{SSP}})^2}{(\sigma_i^{\mathrm{obs}})^2}, \quad (3)$$

where $\mathrm{color}_i^{\mathrm{obs}}$ and $\mathrm{color}_i^{\mathrm{SSP}}$ are the observed and synthetic colors, respectively, σ_i^{obs} is the uncertainty of $\mathrm{color}_i^{\mathrm{obs}}$, and the index i runs over the number of colors, such as F300W − r (when the GC candidate is inside the F300W image), $u-r$, $g-r$, $r-i$, $r-z$, $r-J$, $r-H$, $r-K_s$, $u-g$, and $g-K_s$. As commented above, this last color is particularly useful to break the age-metallicity degeneracy. The ω_i factor represents the weight assigned to each color. After conducting various tests, it was determined that the best fit (minimum value of χ^2) is achieved by assigning equal weight to all colors. Thus, ω_i is set to 1/10 (or 1/9 when F300W is not available), indicating an equal contribution from each color.

We performed a Monte Carlo simulation to derive the physical parameters (log(Age), Z, and A_V) along with their associated uncertainties. This involved introducing Gaussian noise into each observed set of colors, resulting in the generation of 10^4 sets of "observed" colors. The χ^2 minimization method was applied to each set of "observed" colors. This resulted in a Gaussian distribution of ages for the best-fitting models, where the mean (μ_{Age}) represents the log(Age) of the cluster, and its uncertainty is given by the standard deviation (σ_{Age}) of the age distribution. Similarly, the χ^2 minimization process generated 10^4 extinction values, which were used to calculate A_V and its associated uncertainty for each cluster. The metallicity of each cluster corresponds to the metallicity of the model that provides the best fit. The obtained results are presented in Table 10.

Figure 9 displays the results obtained with this SED-fitting analysis for all GC candidates. The observed photometric data are represented by solid circles, while theoretical reddened colors are displayed with open circles. Arrows indicate upper limits in the data.

For the sake of illustration, in each panel we plot a model spectrum[8] of best-fit age, metallicity, and extinction values. Photometric and spectroscopic data are normalized to the flux at the g-band (flux at 4770 Å). The residuals, calculated as $F_{\mathrm{obs}} - F_{\mathrm{SSP}}$, are displayed at the bottom of each panel. The obtained parameters for the remaining clusters are provided in Table 10.

In Figure 10, we compare the ages determined from the SED-fitting procedure with the spectroscopic ages for the eight clusters in common. Two of the clusters inferred as classical GCs (IDs 8 and 20) using the spectroscopic ages have ages log(Age) > 9.90 with the SED method. The derived metallicities of these two clusters are also among the lowest, which authenticates the values derived from the SED-fitting method. For the other six clusters classified as IACs spectroscopically, the SED-fitting derived ages are also consistent with them being younger than classical GCs, with the SED-fitting derived ages systematically higher by up to 0.3 dex. Among the remaining nine clusters without spectroscopic data, one (ID 38) is likely a classical GC (log(Age) $>10.05 \pm 0.10$; $Z = 0.001$), with the rest being IACs with a mean age of 4 Gyr and $Z \lesssim 0.004$. The derived $A_V \lesssim 1$ mag.

[8] SSP models provided by A. Bressan (2024, private communication).

Table 10
Physical Parameters Determined with SED-fitting Using Multiband Photometric Data

ID (1)	Z (2)	log(Age) (3)	A_V (4)	χ^2_{min} (5)
8	0.001	9.93 ± 0.10	0.27 ± 0.08	0.88
20	0.001	9.91 ± 0.05	1.17 ± 0.14	8.61
37	0.004	9.63 ± 0.10	1.82 ± 0.19	0.61
38	0.001	10.05 ± 0.10	0.08 ± 0.10	0.04
49	0.001	9.90 ± 0.05	0.61 ± 0.15	1.00
134	0.004	9.69 ± 0.15	1.38 ± 0.17	0.65
176	0.004	9.60 ± 0.05	0.74 ± 0.17	0.84
190	0.001	9.79 ± 0.10	0.22 ± 0.20	0.06
215	0.004	9.60 ± 0.05	0.43 ± 0.24	0.32
297	0.004	9.60 ± 0.05	1.36 ± 0.35	1.42
329	0.004	9.60 ± 0.05	1.98 ± 0.37	1.10
366	0.02	8.36 ± 0.25	0.72 ± 0.25	0.19
376	0.001	9.80 ± 0.05	0.78 ± 0.27	0.25
384	0.008	8.70 ± 0.40	0.22 ± 0.39	0.35
385	0.004	9.60 ± 0.05	0.79 ± 0.24	0.37
390	0.004	9.60 ± 0.05	1.55 ± 0.36	1.56
391	0.004	9.70 ± 0.15	0.09 ± 0.14	0.05

Note. (2) Metallicity, (3) log(Age) (yr), (4) extinction (mag), (5) minimal χ^2 of the best fitting.

Figure 11 shows the age and extinction values of all star clusters, either through spectral analysis when available (eight objects) or through SED-fitting in cases where spectral analysis was not feasible (nine objects). The log(Age) and A_V for both the samples are very similar, which ensures that the conclusions that we derive do not depend on the method of analysis. The bulk of the red clusters are IACs with ages spread around log(Age) ∼9.6, i.e., 4 Gyr. The A_V distribution is dominated by values of <0.5 mag.

4.4. Photometric Mass

The determination of age, metallicity, and A_V for each cluster allows us to determine the photometric mass of the star clusters. We used the relation:

$$M_{\mathrm{F814W,0}} = \mathrm{F814W}_{\mathrm{SSP}}(t) - 2.5 \log\left(\frac{\mathrm{Mass}}{M_\odot}\right), \quad (4)$$

where $M_{\mathrm{F814W,0}}$ is the reddening-corrected absolute magnitude in the F814W filter (see Section 2.1) and $\mathrm{F814W}_{\mathrm{SSP}}(t)$ is the F814W magnitude for a cluster of 1 $M_\odot$ total mass predicted by the SSP model G02 of age t = log(Age). The values of log(Mass), along with all the derived parameters for all clusters, are summarized in Table 11. The implications of these findings will be discussed in the next section.

5. Discussion

Study of the age and metallicity distribution of the surviving population of GCs in galaxies gives useful clues to understand the build-up of galaxies. As outlined in the introduction, in a

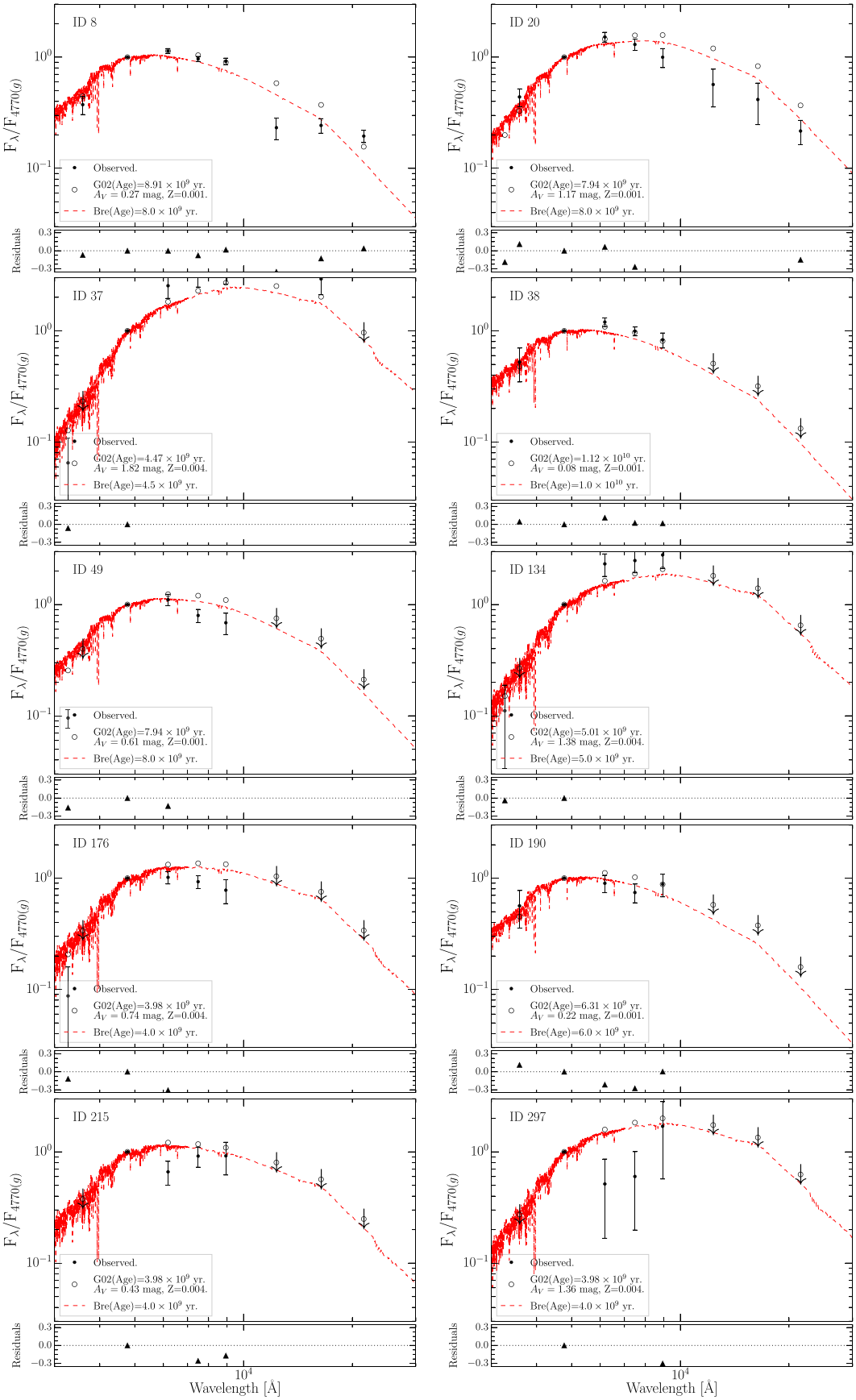

Figure 9. The plots show the results obtained with SED-fitting method using multiband photometry. The photometric data of the best-fitted model (open circles) is compared with the observational data of the cluster (solid circles), arrows represent the upper limit in the respective band. The spectrum of a SSP with physical parameters similar to the best-fitted model is shown (red line) to illustrate the possible form of the spectrum of each cluster. Residuals, $F_{\rm obs} - F_{\rm SSP}$, are shown in the bottom of each panel. Table 10 lists the values of the physical parameters obtained for all clusters.

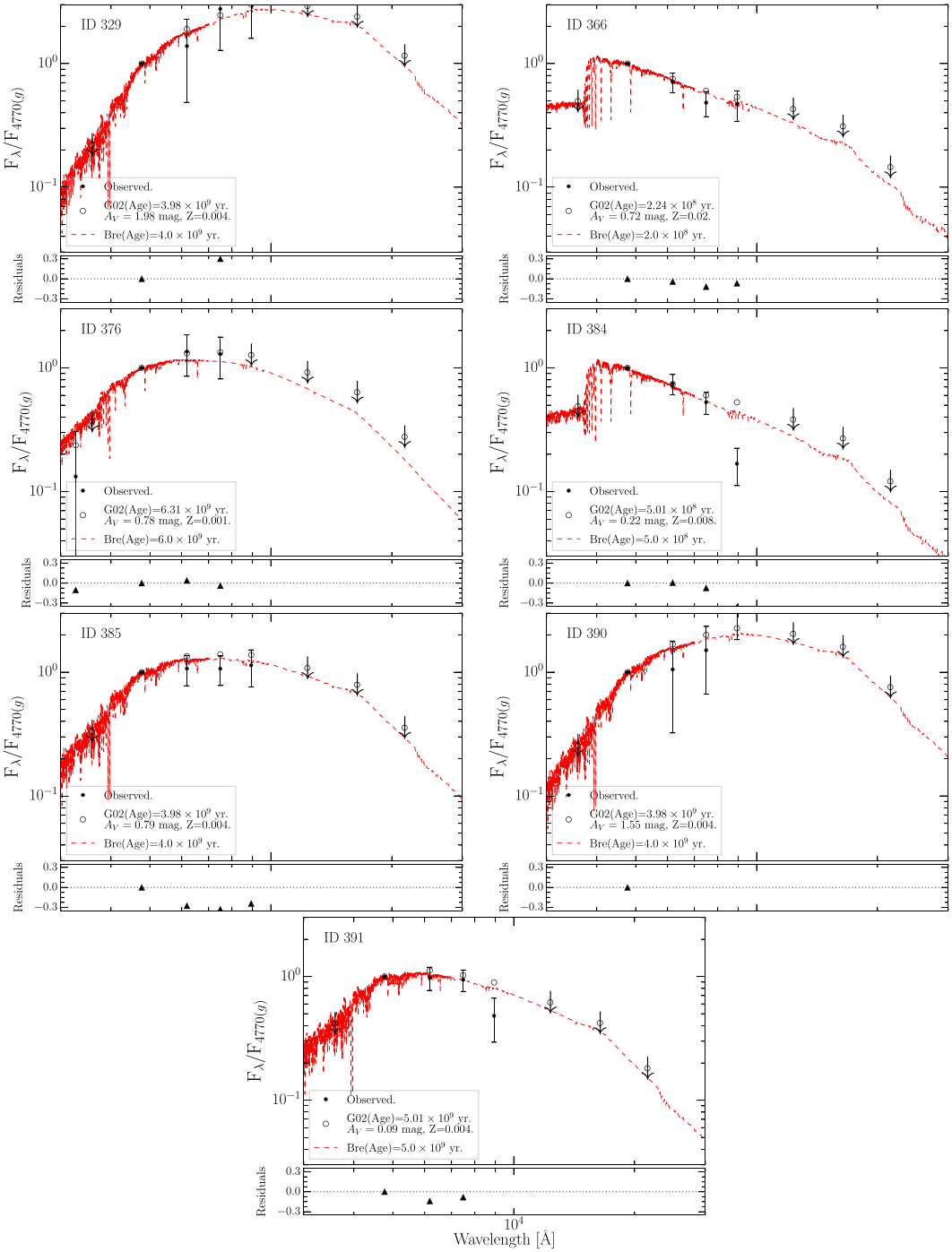

Figure 9. (Continued.)

hierarchical scenario of galaxy formation, metal-poor GCs are formed in the halos of low-mass galaxies (K. Bekki et al. 2008). NGC 3077 is a low-mass local galaxy that has avoided being accreted, and hence it offers an opportunity to test the two-phase formation scenario that has been successful in explaining the observed properties of galaxies (L. Oser et al. 2010). In this section, we discuss the classical GCs and IAC populations in NGC 3077 in the context of hierarchical scenario of galaxy formation and evolution.

Though GCs have been reported previously in NGC 3077 (e.g., D04), this is the first time that their ages and metallicities have been confirmed through spectroscopy. Additionally, we discover an important population of IACs with an age around 5 Gyr. In Figure 12, all clusters analyzed in this work are spatially displayed in the galaxy, symbol shape is for age: circles for classical GCs (age $>$ 10 Gyr), squares for IACs (age $<$ 10 Gyr); while color is for metallicity: red for metal-poor ([Fe/H] < -1) and blue for metal-rich ([Fe/H] > -1). Further details of these clusters will be discussed below.

5.1. Properties of Classical GCs and IACs

The three classical GCs in NGC 3077, namely IDs 8, 20, and 38, are old (age $>$ 10 Gyr), metal-poor ([Fe/H] < -1.0), and

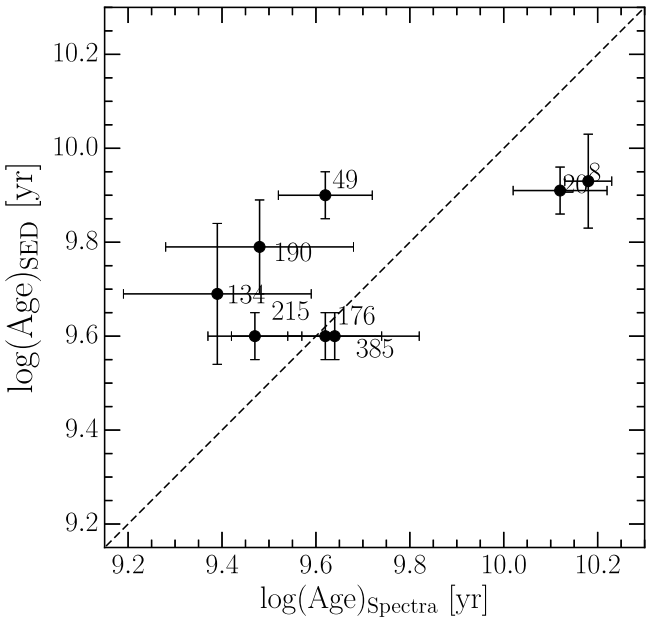

Figure 10. Comparison of log(Age) obtained through two methods: spectra analysis (*x*-axis) and SED-fitting (*y*-axis). The dashed line represents a one-to-one correspondence.

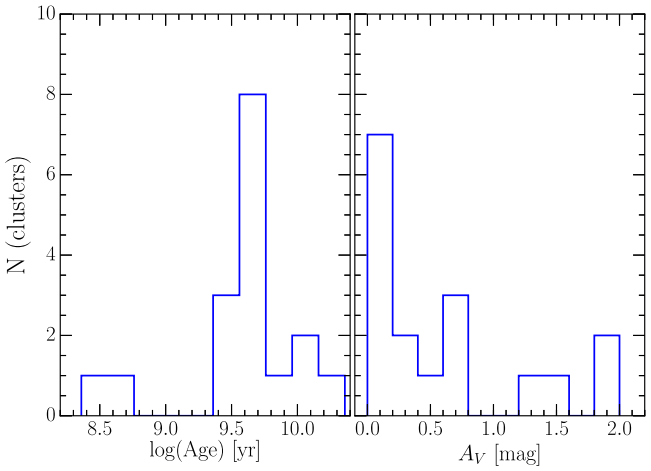

Figure 11. Histograms for log(Age) and A_V, primarily derived through spectral analysis when available and through SED-fitting in cases where spectral analysis was not feasible. Distribution of log(Age) exhibits an important population of IACs (age $\lesssim$5 Gyr) together with the classical GCs (Age >10 Gyr).

massive (mass $>10^5 M_\odot$), characteristics similar to those found in GCs of the Milky Way (MW, W. E. Harris 1996). Their absolute magnitudes are on the brighter side of the turnover magnitude of $M_{V,0} = -7.4$ mag for GCs in the MW and spiral galaxies (L. Lomeli-Nunez et al. 2022). The remaining 14 clusters exhibit intermediate ages, with the majority having ages between ∼2 and 6 Gyr, with a couple of them as young as ∼500 Myr. NGC 3077 is not alone in having more IACs than GCs. For example, the red clusters of LMC are ∼3 Gyr old (S. van den Bergh 1991). We here compare the properties of classical GCs and IACs in NGC 3077 to the properties of the population of old clusters in the MW and irregular galaxies.

In Figure 13, we show the distribution of mass and metallicity against the age (left-hand panels) and the galactocentric distance (R_G) of both the GC (red circles) and IAC (blue squares) populations studied in this work together with the Galactic GCs (black points) and clusters of LMC/SMC (inverted and green triangles, respectively).

In the left-hand panels, a clear correlation is observed between mass and age. However, we should keep in mind that the plotted mass is the photometric mass. For a fixed detection limit, the minimum mass that can be detected increases with age, which explains the absence of old low-mass clusters. So, the observed trend indicates that the most massive cluster formed in recent times is of lower mass as compared to those formed in the earliest epochs of galaxy formation. The right-hand panels reveal that there is no galactocentric distance dependence of the mass and metallicity of the old clusters in NGC 3077.

The three classical GCs are situated at different projected distances from the galaxy center, as depicted in the right-hand panels of Figure 13. The most massive GC in this analysis, ID 8, is located in the northwest direction from the center of NGC 3077 toward M81. This GC has a photometric mass of $\sim 1.1 \times 10^6 M_\odot$ which is comparable to the reported mass of ω Cen (M54, W. E. Harris 1996), and to the most massive GC found in irregular galaxies such as NGC 4449 (F. Annibali et al. 2018).

The availability of radial velocities of IACs allows us to address the question of whether they are in the disk or halo of NGC 3077. F. Walter et al. (2002) analyzed the H I, CO, and Hα kinematics of NGC 3077. They found the H I and CO gas within 70 km s^{-1} of the systemic velocity. The Hα velocity on the other hand extends to 100 km s^{-1}. It is likely that the Hα velocities have a component from outflowing gas, and hence serve as a maximum upper limit for the rotationally supported objects in the disk of NGC 3077. The measured radial velocities of IACs are well within the range of velocities expected for rotating systems in the disk of NGC 3077. In Figure 14, we plot the absolute value of the rotation velocities of IACs (squares) and GCs (red solid circles) after subtracting the systemic velocity as a function of galactocentric distance, both quantities without any corrections for the inclination. An approximate H I rotation curve from F. Walter et al. (2002) in the inner part is shown by a straight line. Except two IACs (IDs 297 and 176), the rest have rotation velocities of 70 ± 10 km s^{-1} similar to the H I velocities. This suggests that IACs are located in the disk of the galaxy at the flat part of the rotation curve. Two possible outliers are IDs 297 and 176. These two objects might not be formed in situ, and instead could be accreting into NGC 3077. Interestingly, the two GCs also have radial velocities consistent with a flat rotation curve.

The IACs span a wide range of metallicities and show an age–metallicity relation with the two youngest clusters being the most metal-rich and three of the oldest IACs (IDs 49, 190, and 376) with [Fe/H] ~ -1.31 are as metal-poor as the three GCs in NGC 3077. NGC 3077 is not the first case of a metal-poor IAC; the metallicity of NGC 339, an IAC (∼6 Gyr old) in the SMC is as metal-poor as its oldest cluster, NGC 121. The observed range of metallicities is in the range of metallicities of metal-rich MW GCs. The median metallicity of [Fe/H] $= -0.71$ for our sample of IACs is similar to the mean metallicity of IACs of the central regions of the SMC (W. Narloch et al. 2021) and of the disk arms and periphery of the LMC (W. Narloch et al. 2022). Measured [α/Fe] for our sample of GCs and IACs cover a wide range of values between −0.04 and 0.45, with no tendency for the oldest metal-poor clusters to have the highest α-enhancement. In fact, the two

Table 11
Derived Parameters for Clusters in NGC 3077

ID (1)	A_V (2)	$M_{F814W,0}$ (3)	$M_{V,0}$ (4)	[Fe/H] (5)	log(Age) (6)	log(Mass) (7)
8	0.56 ± 0.03	-9.68 ± 0.02	-8.72	-1.13 ± 0.11	10.18 ± 0.05	$6.05^{+0.04}_{-0.04}$
20	0.12 ± 0.12	-8.59 ± 0.07	-7.63	-1.06 ± 0.14	10.12 ± 0.10	$5.62^{+0.04}_{-0.04}$
37	1.82 ± 0.19	-9.49 ± 0.11	-8.49	-0.71 ± 0.16	9.63 ± 0.10	$5.64^{+0.03}_{-0.05}$
38	0.08 ± 0.10	-8.47 ± 0.06	-7.51	-1.31	10.05 ± 0.10	$5.53^{+0.04}_{-0.07}$
49	0.00 ± 0.03	-8.19 ± 0.02	-7.19	-1.49 ± 0.16	9.62 ± 0.10	$5.12^{+0.04}_{-0.01}$
134	0.37 ± 0.15	-8.25 ± 0.09	-7.23	-0.71	9.39 ± 0.20	$5.05^{+0.16}_{-0.15}$
176	0.00 ± 0.03	-8.14 ± 0.02	-7.15	-0.71	9.62 ± 0.20	$5.10^{+0.17}_{-0.09}$
190	0.00 ± 0.03	-7.96 ± 0.03	-6.92	-1.32 ± 0.21	9.48 ± 0.20	$5.03^{+0.06}_{-0.16}$
215	0.00 ± 0.03	-8.02 ± 0.02	-6.99	-0.86 ± 0.16	9.47 ± 0.10	$5.05^{+0.01}_{-0.09}$
297	1.36 ± 0.35	-7.86 ± 0.21	-6.86	-0.69 ± 0.24	9.60 ± 0.05	$4.99^{+0.05}_{-0.01}$
329	1.98 ± 0.37	-8.05 ± 0.22	-7.06	-0.71	9.60 ± 0.05	$5.07^{+0.05}_{-0.01}$
366	0.72 ± 0.25	-7.44 ± 0.16	-7.01	0.0	8.36 ± 0.25	$4.19^{+0.15}_{-0.21}$
376	0.78 ± 0.27	-7.63 ± 0.16	-6.67	-1.31	9.80 ± 0.05	$4.98^{+0.07}_{-0.03}$
384	0.22 ± 0.39	-6.75 ± 0.24	-6.11	-0.40	8.70 ± 0.40	$4.02^{+0.16}_{-0.27}$
385	0.62 ± 0.03	-7.54 ± 0.05	-6.55	-0.85 ± 0.12	9.64 ± 0.10	$4.92^{+0.08}_{-0.06}$
390	1.55 ± 0.36	-7.31 ± 0.21	-6.31	-0.71	9.60 ± 0.05	$4.77^{+0.05}_{-0.01}$
391	0.09 ± 0.14	-6.59 ± 0.09	-5.58	-0.71	9.70 ± 0.15	$4.57^{+0.12}_{-0.08}$

Note. (2) Extinction of cluster in (mag), (3) absolute magnitude in F814W band corrected by extinction using C89 law, (4) magnitude in V band also extinction corrected, $M_{V,0} = M_{F814W,0} + (V-I)(t)_{SSP}$, where $(V-I)(t)_{SSP}$ is the color of G02 models, (5) metallicity in terms of [Fe/H] (see e.g., http://miles.iac.es/pages/ssp-models.php miles.iac.es/pages/ssp models for equivalence), (6) log(Age) in (yr), (7) photometric log(Mass) in ($M_\odot$).

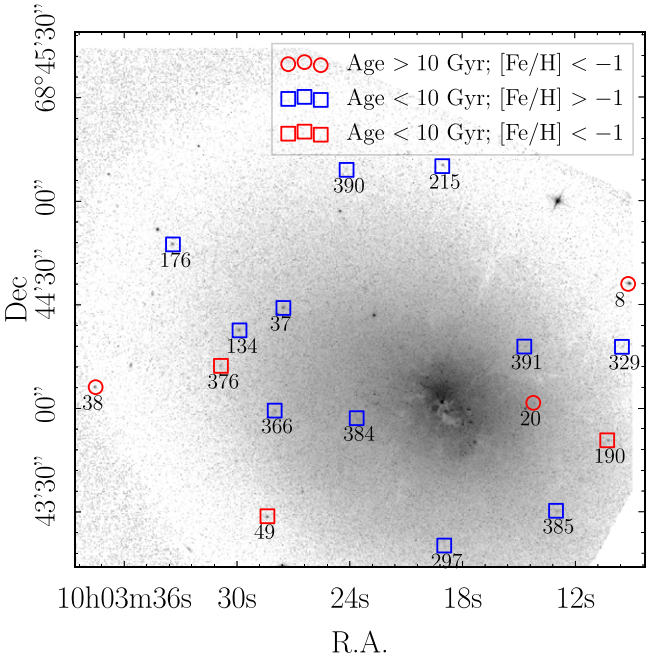

Figure 12. Spatial distribution of all clusters analyzed in this work, with the shapes and color of the symbols indicating their age and metallicities, respectively: circles for classical GCs (age > 10 Gyr), squares for IACs (age < 10 Gyr); red for metal-poor ([Fe/H] < −1) and blue for metal-rich ([Fe/H] > −1). The three classical GCs are metal-poor, whereas the majority of the IACs are metal-rich. North is at the top and East is to the left.

clusters IDs 385 and 215 with highest α-enhancements are metal-rich and are of 3 to 4 Gyr age. Three LMC clusters (NGC 1786, NGC 2210, and NGC 2257) have similarly high α-enhancements, but they are old and metal-poor ([Fe/H] ~ -1.8; A. Mucciarelli et al. 2010). These metal-rich, α-enhanced IACs are not expected in the standard chemical evolution models of galaxies (e.g., I. Minchev et al. 2013). Observations of more clusters would be required in order to postulate alternative scenarios of chemical evolution.

In summary, all clusters older than 10 Gyr in NGC 3077 are metal-poor, suggesting that they most likely formed in metal-poor satellite galaxies and accreted later into NGC 3077 in the second phase of galaxy formation (L. Oser et al. 2010). At the same time NGC 3077 had a major cluster formation event as recently as 4 Gyr ago, which contains both metal-poor and metal-rich clusters. The cluster formation events are related to accretion of satellite galaxies, suggesting that the accretion phase lasted well into $z < 1$ epochs. Such an extended accretion phase is consistent with the results of simulations by L. Oser et al. (2010), who found accretion-driven in situ star formation extending all the way to $z < 1$ in low-mass galaxies. The same models also predict a larger fraction of older clusters to be metal-rich in low-mass galaxies as compared to those in massive galaxies. However, NGC 3077 lacks such metal-rich old clusters. The absence of metal-rich old clusters is a typical property of irregular galaxies such as the LMC and SMC (M. A. Beasley 2020), which suggests that NGC 3077 has a formation history similar to these dwarf galaxies rather than the low-mass galaxies modeled by L. Oser et al. (2010).

5.2. On the Nature of NGC 3077

NGC 3077 is a low-mass dusty star-forming galaxy morphologically classified as Irr II galaxy (A. Sandage 1961), much like M82, the well-known starburst galaxy in the M81 group. Galaxies classified as Irr II do not follow the normal relations obeyed by the galaxies along the Hubble Sequence (e.g., A. Sandage et al. 1975). It is understood that the current appearance is a result of recent interaction events. The galaxies M81, M82 and NGC 3077 had gone through a close interaction around 300 Myr ago, which has left behind streams of H I connecting these galaxies (M. S. Yun 1999). The interaction brought fresh gas into

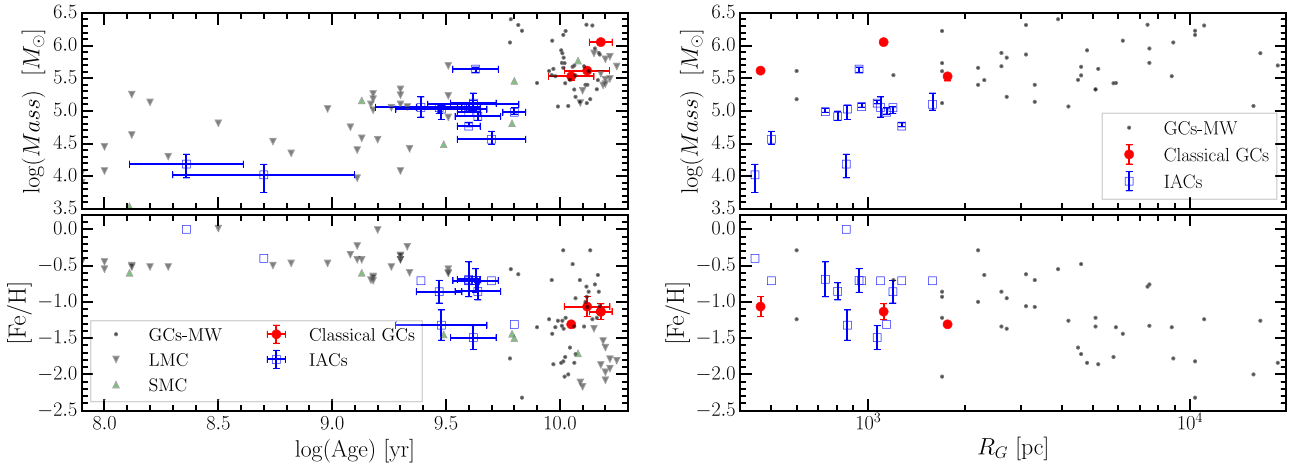

Figure 13. Diagrams for all clusters studied in this work, classical GCs (red circles) and IACs (blue squares). (Left-hand panels) log(Mass) and [Fe/H] are plotted against log(Age), together with Galactic GCs (black points; W. E. Harris 1996; E. Cezario et al. 2013); LMC clusters (inverted triangles; J. F. C. Santos 2004; D. E. McLaughlin & R. P. van der Marel 2005; P. M. Pessev et al. 2006; A. Mucciarelli et al. 2010; and references therein; H. Baumgardt et al. 2013; A. V. Ahumada et al. 2019), and SMC (green triangles; P. M. Pessev et al. 2006; K. Glatt et al. 2011; M. Gatto et al. 2021). (Right-hand panels) log(Mass) and [Fe/H] plotted against R_G, together with Galactic GCs (W. E. Harris 1996; E. Cezario et al. 2013).

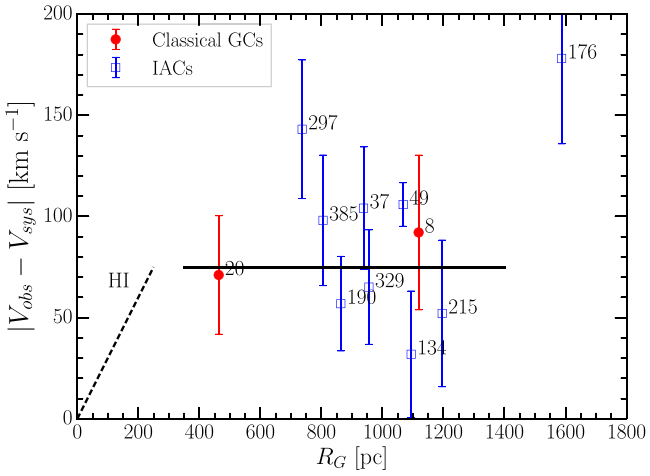

Figure 14. Rotation velocities of IACs (squares) and GCs (red solid circles) against R_G with the average velocity shown by the solid line. An approximate H I rotation curve from F. Walter et al. (2002) in the inner part is shown by a dashed line. Except for IDs 297 and 176, the velocity of the rest of IACs are consistent with a flat rotation curve.

NGC 3077, leading to its current nuclear star formation activity (L. Benacchio & G. Galletta 1981).

The nature of NGC 3077 before its most recent interaction with members of M81 group is still unclear. J. S. Price & C. A. Gullixson (1989) suggested that it was most likely a dwarf elliptical (dE) galaxy, similar to M31's companion NGC 185. D04 used the *K*-band radial surface brightness profiles, which are not greatly affected by the post-interaction star formation, and hence trace the preinteraction morphology, to test the hypothesis of dE origin. He found that the *K*-band radial surface brightness profiles are similar to that of NGC 205, another dE companion of M31.

The old stellar populations hold valuable insights into the early nature of galaxies. S. Okamoto et al. (2023) found that the metallicity distribution function of resolved old stellar populations of NGC 3077 is similar to that of the dE NGC 185 (D. Crnojevic et al. 2014), which suggests a dE origin for NGC 3077. The GC population offers an alternative way to address the nature of the preinteraction galaxy. If NGC 3077 was a dE galaxy, it would be expected to have a specific frequency of GCs, S_N, of greater than 2 (W. E. Harris 1991). This amounts to more than 10 GCs in NGC 3077.

Our findings of only three classical GCs give us $S_N = 0.7$, which is well below the values expected for dEs but consistent with values reported by W. E. Harris (1991) and I. Y. Georgiev et al. (2008) for irregular galaxies with similar M_V magnitude. D04 reported 12 GCs in NGC 3077 using ground-based NIR images, corresponding to $S_N = 2.5$, a number close to that expected if it was a dE galaxy. However, our analysis of these 12 objects reported as GCs using the recently available GAIA parameters (see Figure 4) suggests only two objects, both classified by us as classical GCs, are genuine GCs, the rest are foreground Galactic stars. The FWHM of those stars that fall inside the HST/ACS field of view (FoV) also satisfy our criteria as foreground stars at the HST resolution. Hence, the use of GAIA parameters would lower the S_N value from D04 study close to 0.7.

The S_N-based arguments to infer intrinsic morphology of galaxies suffer from a caveat: none of the objects in the study of W. E. Harris (1991) were confirmed as classical metal-poor old GCs by detailed studies such as carried out here. Hence, if we relax the definition, most if not all of our 17 GC candidates would be classified as GCs, in which case the S_N for NGC 3077 could be in the range of values expected for dE systems. These numbers could be lower limits if some GCs were stripped during the interaction event that the members of M81 group had around 300 Myr ago. Massive SSCs that survive for gigayears are usually formed in intense star formation bursts, associated with past interaction and merging events. Hence, the presence of a rich population of 34 Gyr IACs in NGC 3077 suggests major events of star formation at these look back times. Study of star formation histories (SFHs) of dE galaxies suggests that these galaxies formed bulk of their stars early in their lives, later on forming stars at low rates (M. Koleva et al. 2009; D. R. Weisz et al. 2014). The presence of a rich population of IACs suggests an SFH akin to irregular galaxies. Hence, if the preinteraction NGC 3077 was indeed a dE, the IACs would not have been formed in situ in NGC 3077 and instead acquired through accretion.

6. Summary and Conclusions

We here present the results of an elaborate search for GC candidates in the HST/ACS images of the nearby Irr II galaxy NGC 3077. New spectroscopic observations using the OSIRIS spectrograph at the GTC were carried out for a subsample of the selected candidates to obtain radial velocity, age, metallicity, extinction, and photometric mass. Complementary data from SDSS and 2MASS missions, as well as proper motion and other parameters from GAIA mission were compiled to reject stars and other noncluster candidates to define a sample of 17 genuine GC-like objects. We find that three of these objects have characteristics of classical metal-poor ($[Fe/H] < -1.0$) old (age > 10 Gyr) GCs. Most of the remaining objects are of intermediate age, metal-rich ($[Fe/H] > -1.0$) clusters. The measured radial velocities of IACs are well within the range of velocities expected for rotating systems in the disk of NGC 3077. The metallicities, ages, and masses of GCs and IACs in NGC 3077 compare well with those properties in the nearby dwarf galaxies, the LMC and SMC.

The calculated value of S_N is 0.7, which is similar to the values obtained in previous studies for irregular galaxies and suggests that the preinteraction galaxy was actively forming stars and SSCs and is unlikely to be a dE as suggested in some of the previous studies.

Acknowledgments

P.A.O. thanks the Mexican CONAHCYT for the scholarship grant which enabled the realization of this work (doctoral fellowship 345527), and L.L.N. thanks Fundação de Amparo à Pesquisa do Estado do Rio de Janeiro (FAPERJ) for granting the postdoctoral research fellowship E-40/2021(280692). We are grateful for the anonymous referee whose thoughtful suggestions helped to improve the presentation of the results obtained in this work.

This study is based on observations carried out with the NASA/ESA Hubble Space Telescope, which was accessed using the MAST interface (which is available on Zenodo under an open-source Creative Commons Attribution license: doi:10.17909/d7vy-5145). We also used Sloan Digital Sky Survey V data (SDSS), which was funded by the Alfred P. Sloan Foundation, the Heising-Simons Foundation, the National Science Foundation, and the Participating Institutions. SDSS acknowledges support and resources from the Center for High-Performance Computing at the University of Utah. SDSS telescopes are located at Apache Point Observatory, funded by the Astrophysical Research Consortium and operated by New Mexico State University, and at Las Campanas Observatory, operated by the Carnegie Institution for Science. The SDSS website is www.sdss.org. This publication makes use of data products from the Two Micron All Sky Survey, which is a joint project of the University of Massachusetts and the Infrared Processing and Analysis Center/California Institute of Technology, funded by the National Aeronautics and Space Administration and the National Science Foundation. This work has also made use of data from the European Space Agency (ESA) mission Gaia (https://www.cosmos.esa.int/gaia), processed by the Gaia Data Processing and Analysis Consortium (DPAC, https://www.cosmos.esa.int/web/gaia/dpac/consortium). Funding for the DPAC has been provided by national institutions, in particular the institutions participating in the Gaia Multilateral Agreement.

ORCID iDs

P. A. Ovando https://orcid.org/0000-0002-4437-347X
Y. D. Mayya https://orcid.org/0000-0002-4677-0516
L. H. Rodríguez-Merino https://orcid.org/0000-0003-0961-3105
L. Lomelí-Nuñez https://orcid.org/0000-0003-2127-2841
B. Cuevas-Otahola https://orcid.org/0000-0002-1046-1500
D. Rosa-González https://orcid.org/0000-0003-1327-0838

References

Abazajian, K., Adelman-McCarthy, J. K., Agüeros, M. A., et al. 2003, AJ, 126, 2081
Adamo, A., Bradley, L. D., Vanzella, E., et al. 2024, Natur, 632, 513
Ahumada, A. V., Vega-Neme, L. R., Clariá, J. J., & Minniti, J. H. 2019, PASP, 131, 024101
Alamo-Martínez, K. A., Chies-Santos, A. L., Beasley, M. A., et al. 2021, MNRAS, 503, 2406
Annibali, F., Morandi, E., Watkins, L. L., et al. 2018, MNRAS, 476, 1942
Asa'd, R. S. 2014, MNRAS, 445, 1679
Ashman, K. M., & Zepf, S. E. 1998, Globular Cluster Systems (Cambridge: Cambridge Univ. Press)
Babusiaux, C., Fabricius, C., Khanna, S., et al. 2023, A&A, 674, A32
Bastian, N., Niederhofer, F., Kozhurina-Platais, V., et al. 2016, MNRAS, 460, L20
Baumgardt, H., Parmentier, G., Anders, P., & Grebel, E. K. 2013, MNRAS, 430, 676
Beasley, M. A. 2020, in Reviews in Frontiers of Modern Astrophysics; From Space Debris to Cosmology, ed. P. Kabáth, D. Jones, & M. Skarka (Berlin: Springer), 245
Beasley, M. A., Trujillo, I., Leaman, R., & Montes, M. 2018, Natur, 555, 483
Bekki, K., Yahagi, H., Nagashima, M., & Forbes, D. A. 2008, MNRAS, 387, 1131
Benacchio, L., & Galletta, G. 1981, ApJL, 243, L65
Bertin, E., & Arnouts, S. 1996, A&AS, 117, 393
Blakeslee, J. P., Cho, H., Peng, E. W., et al. 2012, ApJ, 746, 88
Bressan, A., Marigo, P., Girardi, L., et al. 2012, MNRAS, 427, 127
Brodie, J. P., & Huchra, J. P. 1990, ApJ, 362, 503
Brodie, J. P., & Strader, J. 2006, ARA&A, 44, 193
Burstein, D., Faber, S. M., Gaskell, C. M., & Krumm, N. 1984, ApJ, 287, 586
Caldwell, N., & Romanowsky, A. J. 2016, ApJ, 824, 42
Calzetti, D., Armus, L., Bohlin, R. C., et al. 2000, ApJ, 533, 682
Calzetti, D., Harris, J., Gallagher, J. S., III, et al. 2004, AJ, 127, 1405
Cardelli, J. A., Clayton, G. C., & Mathis, J. S. 1989, ApJ, 345, 245
Cezario, E., Coelho, P. R. T., Alves-Brito, A., Forbes, D. A., & Brodie, J. P. 2013, A&A, 549, A60
Chies-Santos, A. L., de Souza, R. S., Caso, J. P., et al. 2022, MNRAS, 516, 1320
Crnojevic, D., Ferguson, A. M. N., Irwin, M. J., et al. 2014, MNRAS, 445, 3862
Davidge, T. J. 2004, AJ, 127, 1460
de Vaucouleurs, G. 1959, HDP, 53, 275
de Vaucouleurs, G., de Vaucouleurs, A., Corwin, H. G., Jr, et al. 1991, Third Reference Catalogue of Bright Galaxies. Volume I: Explanations and References. Volume II: Data for Galaxies Between 0^h and 12^h. Vol. III: Data for Galaxies Between 12^h and 24^h (New York: Springer)
Forbes, D. A., Spitler, L. R., Strader, J., et al. 2011, MNRAS, 413, 2943
Freedman, W. L., Hughes, S. M., Madore, B. F., et al. 1994, ApJ, 427, 628
Gaia Collaboration, Prusti, T., de Bruijne, J. H. J., et al. 2016, A&A, 595, A1
Gatto, M., Ripepi, V., Bellazzini, M., et al. 2021, MNRAS, 507, 3312
Georgiev, I. Y., Goudfrooij, P., Puzia, T. H., & Hilker, M. 2008, AJ, 135, 1858
Girardi, L., Bertelli, G., Bressan, A., et al. 2002, A&A, 391, 195
Girardi, L., Bressan, A., Bertelli, G., & Chiosi, C. 2000, A&AS, 141, 371
Glatt, K., Grebel, E. K., Jordi, K., et al. 2011, AJ, 142, 36
Gomez-Gonzalez, V. M. A., Mayya, Y. D., & Rosa-Gonzalez, D. 2016, MNRAS, 460, 1555
González-López lira, R. A., Lomelí-Núñez, L., Álamo-Martínez, K., et al. 2017, ApJ, 835, 184
Harris, J., Calzetti, D., Gallagher, J. S., III, Smith, D. A., & Conselice, C. J. 2004, ApJ, 603, 503

Harris, W. E. 1991, ARA&A, 29, 543
Harris, W. E. 1996, AJ, 112, 1487
Harris, W. E., & van den Bergh, S. 1981, AJ, 86, 1627
Hodge, P. W., Dolphin, A. E., Smith, T. R., & Mateo, M. 1999, ApJ, 521, 577
Holmberg, E. 1950, MeLuS, 128, 1
Hughes, A. K., Sand, D. J., Seth, A., et al. 2021, ApJ, 914, 16
Kauffmann, G., & White, S. D. M. 1993, MNRAS, 261, 921
Koleva, M., De Rijcke, S., Prugniel, P., Zeilinger, W. W., & Michielsen, D. 2009, MNRAS, 396, 2133
Krienke, O. K., Jr., & Hodge, P. W. 1974, AJ, 79, 1242
Kroupa, P. 2001, MNRAS, 322, 231
Kruijssen, J. M. D., Pfeffer, J. L., Crain, R. A., & Bastian, N. 2019, MNRAS, 486, 3134
Larsen, S. S., Brodie, J. P., Forbes, D. A., & Beasley, M. A. 2001, AAS Meeting Abstracts, 199, 52.04
Lomeli-Nunez, L., Mayya, Y. D., Rodriguez-Merino, L. H., Ovando, P. A., & Rosa-Gonzalez, D. 2022, MNRAS, 509, 180
Lomelí-Núñez, L., Mayya, Y. D., Rodríguez-Merino, L. H., et al. 2024, MNRAS, 528, 1445
Mayya, Y. D., Bressan, A., Carrasco, L., & Hernandez-Martinez, L. 2006, ApJ, 649, 172
Mayya, Y. D., Romano, R., Rodríguez-Merino, L. H., et al. 2008, ApJ, 679, 404
Mayya, Y. D., Rosa-Gonzalez, D., Santiago-Cortes, M., et al. 2013, MNRAS, 436, 2763
McLaughlin, D. E., & van der Marel, R. P. 2005, ApJS, 161, 304
Minchev, I., Chiappini, C., & Martig, M. 2013, A&A, 558, A9
Mucciarelli, A., Origlia, L., & Ferraro, F. R. 2010, ApJ, 717, 277
Muñoz, R. P., Puzia, T. H., Lançon, A., et al. 2014, ApJS, 210, 4
Nantais, J. B., & Huchra, J. P. 2010, AJ, 139, 2620
Narloch, W., Pietrzyński, G., Gieren, W., et al. 2021, A&A, 647, A135
Narloch, W., Pietrzyński, G., Gieren, W., et al. 2022, A&A, 666, A80
Notni, P., Karachentsev, I. D., & Makarova, L. N. 2004, AN, 325, 307
Okamoto, S., Arimoto, N., Ferguson, A. M. N., Irwin, M. J., & Žemaitis, R. 2023, ApJ, 952, 77
Oser, L., Ostriker, J. P., Naab, T., Johansson, P. H., & Burkert, A. 2010, ApJ, 725, 2312
Pan, J., Bell, E. F., Smercina, A., et al. 2022, MNRAS, 515, 48
Parisi, M. C., Geisler, D., Carraro, G., et al. 2014, AJ, 147, 71
Pérez, E., Cid Fernandes, R., González Delgado, R. M., et al. 2013, ApJL, 764, L1
Pessev, P. M., Goudfrooij, P., Puzia, T. H., & Chandar, R. 2006, AJ, 132, 781
Pfeffer, J., Kruijssen, J. M. D., Crain, R. A., & Bastian, N. 2018, MNRAS, 475, 4309
Price, J. S., & Gullixson, C. A. 1989, ApJ, 337, 658
Rodríguez-Merino, L. H., Rosa-González, D., & Mayya, Y. D. 2011, ApJ, 726, 51
Sanchez-Blazquez, P., Peletier, R. F., Jimenez-Vicente, J., et al. 2006, MNRAS, 371, 703
Sandage, A. 1961, The Hubble Atlas of Galaxies (Washington, DC: Carnegie Institution)
Sandage, A., Sandage, M., & Kristian, J. 1975, Galaxies and the Universe (Chicago, IL: Univ. Chicago Press)
Santiago-Cortés, M., Mayya, Y. D., & Rosa-González, D. 2010, MNRAS, 405, 1293
Santos, J. F. C., & Piatti, A. E, J. 2004, A&A, 428, 79
Schiavon, R. P., Rose, J. A., Courteau, S., & MacArthur, L. A. 2005, ApJS, 160, 163
Schlegel, D. J., Finkbeiner, D. P., & Davis, M. 1998, ApJ, 500, 525
Searle, L., & Zinn, R. 1978, ApJ, 225, 357
Skrutskie, M. F., Cutri, R. M., Stiening, R., et al. 2006, AJ, 131, 1163
Strader, J., Seth, A. C., & Caldwell, N. 2012, AJ, 143, 52
Thomas, D., Maraston, C., & Bender, R. 2003, MNRAS, 339, 897
Tody, D. 1986, Proc. SPIE, 627, 733
Trager, S. C., Worthey, G., Faber, S. M., Burstein, D., & González, J. J. 1998, ApJS, 116, 1
Usher, C., Forbes, D. A., Brodie, J. P., et al. 2012, MNRAS, 426, 1475
van den Bergh, S. 1991, ApJ, 369, 1
van der Hulst, J. M. 1979, A&A, 75, 97
VandenBerg, D. A., Brogaard, K., Leaman, R., & Casagrande, L. 2013, ApJ, 775, 134
Vazdekis, A., Sánchez-Blázquez, P., Falcón-Barroso, J., et al. 2010, MNRAS, 404, 1639
Walter, F., Weiss, A., Martin, C., & Scoville, N. 2002, AJ, 123, 225
Wang, S., Ma, J., & Liu, J. 2019, A&A, 623, A65
Weisz, D. R., Dolphin, A. E., Skillman, E. D., et al. 2014, ApJ, 789, 147
Whitmore, B. C., Chandar, R., Bowers, A. S., et al. 2014, AJ, 147, 78
Wisniewski, W. Z., & Kleinmann, D. E. 1968, AJ, 73, 866
Worthey, G., Faber, S. M., Gonzalez, J. J., & Burstein, D. 1994, ApJS, 94, 687
Yun, M. S. 1999, IAU Symp. 186, Galaxy Interactions at Low and High Redshift, ed. J. E. Barnes & D. B. Sanders (Cambridge: Cambridge Univ. Press), 81
Yun, M. S., Ho, P. T. P., & Lo, K. Y. 1994, Natur, 372, 530
Zepf, S. E., & Ashman, K. M. 1993, MNRAS, 264, 611